

# DOCTORAL DISSERTATION PROPOSAL

---

## Numerical Simulation of Synthetic, Buoyancy-Induced Columnar Vortices

---

NICHOLAS MALAYA

DEPARTMENT OF MECHANICAL ENGINEERING  
UNIVERSITY OF TEXAS AT AUSTIN

*Committee:*

Dr. Robert D. Moser  
*Advisor*

Department of Mechanical Engineering  
and Institute for Computational  
Engineering and Science

Dr. David Bogard  
Department of Mechanical Engineering

Dr. Ofodike A. Ezekoye  
Department of Mechanical Engineering

Dr. Charles S. Jackson  
Jackson School of Geosciences

Dr. Todd A. Oliver  
Institute for Computational Engineering  
and Science

## **Abstract**

Much of the solar energy incident on the Earth's surface is absorbed into the ground, which in turn heats the air layer above the surface. This buoyant air layer contains considerable gravitational potential energy. The energy in this layer can drive the formation of columnar vortices ("Dust Devils") which arise naturally in the atmosphere. A new energy harvesting approach makes use of this phenomena by creating and anchoring the vortices artificially and extracting energy from them. In the research proposed here, we will explore the characteristics of these vortices through numerical simulation. Computational models of the turning vane system which generates the vortex and the turbine used to extract energy have been developed and are presented here. These models have been tested against available experimental measurements. Preliminary results from these studies are also presented, as well as initial details of the columnar vortex structure. In addition, we introduce the approach used to optimize the system configuration to maximize the power extraction. The objective of this work is to explore a wide variety of configurations to assess the technological feasibility of the overall endeavor.

# Contents

<b>1</b>	<b>Introduction / Executive Summary</b>	<b>3</b>
<b>2</b>	<b>Physics of Dust Devils</b>	<b>5</b>
2.1	Phenomenological Character of Dust Devils . . . . .	5
2.2	Estimate of Energy Scaling . . . . .	6
2.3	Dust Devil Generation Concept . . . . .	9
<b>3</b>	<b>Mathematical Modeling</b>	<b>12</b>
3.1	Equations of Fluid Motion . . . . .	13
3.2	Viscosity Model . . . . .	13
3.3	Eddy Viscosity in the Device . . . . .	16
3.4	Vane and Turbine Representation . . . . .	17
3.5	Solid Surface Representation . . . . .	18
3.6	Separation Model . . . . .	18
3.7	Effect of Surface Roughness . . . . .	21
3.8	Simulation Geometry and Boundary Conditions . . . . .	21
<b>4</b>	<b>Computational Methods and Software</b>	<b>27</b>
4.1	Discretization Scheme . . . . .	27
4.2	Mesh Discretization . . . . .	28
4.3	Software Stack . . . . .	30
4.4	Tool Chain and Simulation Custodianship . . . . .	30
<b>5</b>	<b>Validation</b>	<b>32</b>
5.1	Thermal-Only Validation . . . . .	33
5.2	Wind Cases . . . . .	36
5.3	Field Configurations . . . . .	36
<b>6</b>	<b>Preliminary Results</b>	<b>40</b>
6.1	Thermal Only . . . . .	40
6.2	Wind . . . . .	42
6.3	Optimization . . . . .	43
<b>7</b>	<b>Proposed Research Campaign</b>	<b>51</b>
7.1	Proposed Timeline . . . . .	53
<b>A</b>	<b>Course list</b>	<b>56</b>
<b>B</b>	<b>Stabilization and Weak Formulation</b>	<b>57</b>
B.1	Weak Formulation of Equations of Interest . . . . .	57
B.2	The operators L and S . . . . .	58
B.3	Tau stabilization terms . . . . .	61

# 1 Introduction / Executive Summary

Renewable energy is critical to our environmental, economic, and national security. Global demand for energy is projected to rise 56% by 2040[1], as is our national reliance on fossil fuel-based power plants for the bulk of our electricity generation. There is a critical need for safe, clean, and cost-effective alternatives to coal, such as wind, solar, hydroelectric, and geothermal power. These technologies will simultaneously reduce carbon dioxide emissions and help position the U.S. as a leader in the global renewable energy industry. This proposal details a research plan to perform a numerical investigation and design optimization of a novel renewable energy concept.

Much of the solar energy incident on the Earth’s surface is absorbed into the ground, which in turn heats the air layer above the surface. This buoyant air layer contains considerable gravitational potential energy. With nearly one-third of global land mass covered by deserts, there are huge untapped regions for capturing solar heat (about  $200 \text{ W/m}^2$  averaged over a 24-hour day, and up to  $1000 \text{ W/m}^2$  peak)[14]. The available power is competitive in magnitude with worldwide power generation from fossil sources. If a technology could effectively extract this energy, it would result in a low-cost, scalable approach to electrical power generation that could create a new class of renewable energy ideally suited for arid regions.

How then, is one to efficiently extract this gravitational potential energy and convert it into usable work? We turn to Nature to provide a guide, with the observation that there are natural objects that provide precisely this mechanism. Namely, naturally occurring “dust devils” characterized by a vertically stratified, ground-heated air layer that produces a coherent columnar vortex. These “dust devil”s are ubiquitous, naturally appearing in regions as diverse as Arizona, Siberia, over water, or even Mars[28, 3, 31]. They are observed to occur over a wide range of length scales (1 - 30 meters) with large variations in velocities (1 to over 40 m/s)[28].

The basic idea behind the proposed energy harvesting approach is to convert the potential energy in this buoyant air layer to kinetic energy in an anchored vortex, and to use that kinetic energy to drive a vertical-axis turbine coupled with an electric generator to produce electrical power. The Solar-Driven Vortex (SoV) phenomena has been demonstrated in an experimental setup by our partners at Georgia Tech. However, to move beyond proof-of-concept, Computational Fluid Dynamics (CFD) is needed to simulate the SoV. Such simulations will provide fundamental insight into the driving dynamics of the system and generate high resolution data, which is experimentally inaccessible, to be used to rapidly

optimize the geometry and configuration of the SoV apparatus.

The objective of this project is to assess the technological feasibility of using synthetic columnar vortices to generate usable energy. This proposal begins in Section 2 with a discussion of the naturally occurring phenomenon, the presently understood dynamics of dust-devils and similar columnar vortices, and the implications for systems designed to generate their synthetic counterparts. In Section 3, we outline a mathematical model of the entire system, and in Section 4, we discuss the algorithms and software implementation used to simulate the system. Section 5 discusses the validation of these results against existing experimental data and high fidelity simulations. Section 6 details the preliminary predictions of system performance in the field, as well as detailing the several examples of a numerical optimization of the apparatus. Finally, with the preceding sections outlining the present simulation capabilities, Section 7 proposes a course of investigation designed to broadly probe the design space and provide a definitive assessment of the technological feasibility of the entire synthetic columnar vortex concept.

## 2 Physics of Dust Devils

This section addresses what is known about naturally occurring dust devils, to motivate how best to *engineer* a synthetic version. It begins with a qualitative discussion of dust-devils, followed by a review of the known physics and pertinent literature review. Finally, it ends with an plan to leverage these physical processes as a method of usable energy generation.

### 2.1 Phenomenological Character of Dust Devils

There is no rigorous definition of a dust devil, despite the fact that the phenomenon is ubiquitous. These whirlwinds have been observed across a wide variety of terrains, climates and even on several other planets[28, 7, 27, 31]. While a precise definition is elusive, several features are characteristic of a dust devil. They are regions of intense vorticity and rotation, coupled with strong upward motions that are strong enough draw and lift particles into the flow. They are self-sustaining vortices that maintains a funnel-like chimney driven by hot air moving both upward and circularly. While they typically survive for only a few minutes, some have been observed to endure for significantly longer. The velocities are typically several meters per second, but dust devils are occasionally strong enough to cause damage and injury, with some reaching F1 on the Fujita Tornado intensity scale[11], with velocities between 33 and 49 m/s. Diameters range from about one meter to greater than thirty. Their average height is about thirty meters, but a few have been observed as high as one kilometer or more. They do not appear to have a preferred rotation direction. Although the vertical velocity is predominantly upward, the flow along the a central axis of large dust devils may be downward. Visibly similarly structured phenomena have been observed over water, in intense forest fires, and in cold or freezing environments.

While the phenomenon is pervasive, certain environmental conditions impact the frequency of dust devil formation. Sinclair[28] performed perhaps the most systematic investigation characterizing conditions favorable for formation. He noted that dust devils are most likely to form at solar noon, the time of the greatest incident radiation on the ground. Furthermore, they are more likely to form in locations with a higher surface temperature. Moderate to high wind speeds (2-5 m/s) encourage dust devil genesis, but greater velocities (11 m/s) appear to impede formation. They are more likely to be observed in relatively flat locations, such as deserts.

Numerical simulations of dust devils have been previously reported. However, they are typically large eddy simulations (LES) that point towards the spontaneous occurance of

similar phenomena within existing climate and atmospheric models[17, 33]. Actual measurements made inside a dust devil are limited. The available data hints that dust devils contain two regions: a low surface layer and a higher invisid region. The low surface region is the principle location of radial inflow. At the top of this region the flow reaches its peak velocity, with that peak dropping with increasing height. The strong radial and azimuthal flow is drawn into a low pressure core where it gains vertical velocity. Earlier experimental and computational studies have observed a “two-cell” structure characterized by a cool downdraft in the center of stronger dust devils[33, 29]. It is not clear what generates the azimuthal velocities. It is possible that ambient vorticity in the atmosphere is drawn into the vortex from the far field, and intensifies due to vortex stretching.

The higher region is characterized by a largely invisid potential flow region with warm air rising and circling around a cool, low pressure core. This region is typically many times larger in height than the surface layer. While this region also has radial inflow, it is significantly weaker than the lower region. Previous studies have found this region is relatively well described by a Rankine vortex model[29]. These regions are indicated in a simple cartoon in Figure 1.

## 2.2 Estimate of Energy Scaling

Here we provide a rough estimate of the energy available to a dust devil. There are two objectives of this analysis. The first is to provide justification for the concept of extracting energy from them, with the reasoning that should sufficient energy be available, then attempting to extract it might be worthwhile. The second objective is to provide a simple analysis that can serve as a measure of the efficiency of the generation process, e.g. “What fraction of the available energy are we extracting?”.

At present, we consider only the energy flowing into the entrainment region due to the ambient conditions, in particular, the incoming wind and heat flowing through a cylindrical region. We consider a medium-sized (3m radius) dust devil with an incoming freestream velocity of 5 m/s. The surface temperature is 343 Kelvin, with a specified inflow boundary layer bridging the ground temperature to the ambient air conditions of 313 Kelvin.<sup>1</sup>

There are two forms of energy to consider: kinetic and gravitational potential. First, we examine the kinetic energy flux through the front of the apparatus. The kinetic energy flux

---

<sup>1</sup>These numbers were selected based on information provided by the Georgia Tech field team from measurements performed in Arizona during the summer of 2014.

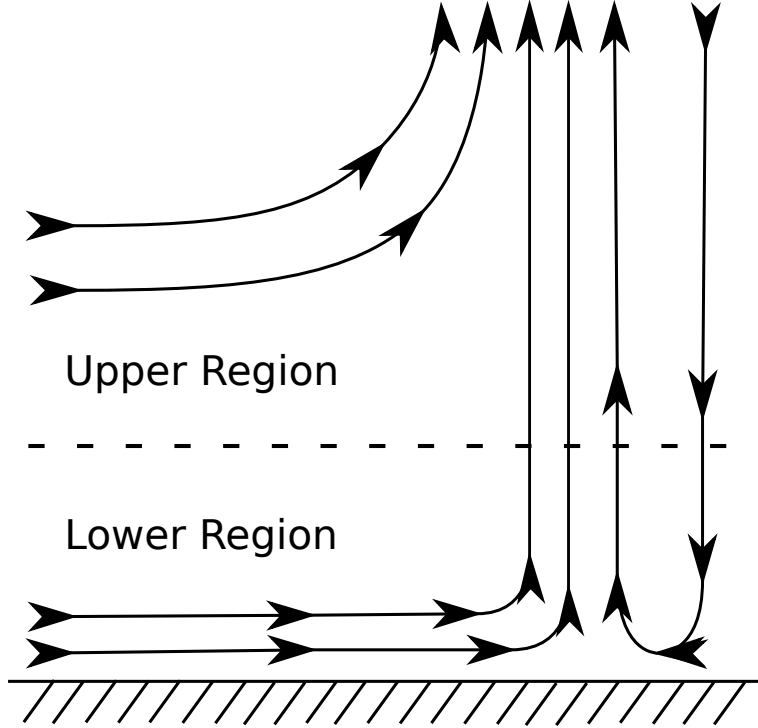


Figure 1: Cartoon of the structure of a dust devil. The lower region is the principle location of radial inflow, with the higher second layer flow becoming entrained by the upwardly circulating vortex. Notice also the downward flow in the center of the vortex.

is a surface integral over the upstream face of the device,

$$KE = \int \frac{\vec{V}^2}{2} \rho \vec{V} \cdot \hat{n} dA.$$

Several simplifying assumptions are made. The freestream velocity is assumed to have no components in the span and height and the variation in height of the streamwise velocity is only due to the thin boundary layer near the ground. The boundary layer profile is modeled using the common 7th power function for a turbulent boundary layer,

$$u(z) = U \min \left( \left( \frac{z}{\delta} \right)^7, 1 \right)$$

where  $U$  is the constant freestream velocity and  $\delta$  the assumed boundary layer thickness.

The result for the kinetic energy is then,

$$KE = R\rho U^3 \left[ z_{\max} - \frac{10}{11}\delta \right].$$

Where  $R$  is the radius of the vortex. Typical values of these quantities are,  $U = 5$  m/s,  $\rho = 1.225$  Kg/m<sup>3</sup>,  $R = 3$  m,  $z_{\max} = 2.5$  m and  $\delta \approx 10$  cm. This provides an estimate of 1144 Watts as the incoming kinetic energy flux.

The gravitational potential energy flux is estimated by integrating the boussinesq potential energy flux over the upstream flow. This is the maximum energy that could be extracted from the flow by an adiabatic redistribution of the density variation from the ambient density of the freestream flow,  $\rho_\infty$ . This potential energy ( $E_p$ ) has the form of a surface integral over the front half of the vanes,

$$E_p = \int u(z)(\rho(z) - \rho_\infty) g z dA.$$

As the density only varies with height, the integral is simplified to only vary in this direction

$$E_p = g \int_0^{z_{\max}} u(z)(\rho(z) - \rho_\infty) z \pi R dz.$$

Using the bousinesq approximation,  $(\rho(z) - \rho_\infty) = \rho_0 \beta \Delta T$ , the integral becomes,

$$E_p = g \pi R \beta \rho_0 \Delta T \int_0^{z_{\max}} u(z) z dz.$$

This is solved to show

$$E_p = g \pi R \beta \rho_0 U \Delta T \left[ \frac{z_{\max}^2}{2} - \frac{7\delta^2}{18} \right].$$

Characteristic values for a dust devil are  $\rho_0 = 1.225$  Kg/m<sup>3</sup>,  $\Delta T = 30$  Kelvin,  $\beta = 0.003194$  (This is  $1/T_{\text{ground}}$ ),  $R = 3$  m,  $z_{\max} = 2.5$  m,  $\delta \approx 10$  cm,  $g = 9.81$  m/s<sup>2</sup>, and a freestream velocity of five meters per second results in an estimate of 34 Watts for the gravitational potential energy.

The majority of the available energy is thus in the kinetic energy of the wind, not the gravitational potential energy of the actual air. However, while the gravitational potential energy is a small fraction of the energy available, that does not imply it is without significant impact. Given the observed increase in dust devil formation during peak thermal gradients,

it is expected to play an important role.

### 2.3 Dust Devil Generation Concept

The preceding discussion suggests that dust devils are carriers of significant levels of ambient kinetic and gravitational potential energy from the environment. This subsection provides a brief discussion of how the physics of dust devils informs the generation of a synthetic variety, that might be used as a means of extracting usable work.

In contrast to the naturally occurring dust devils, our synthetic solar driven vortex (SoV) design makes use of control surfaces. These turning vanes also serve as an anchor for the synthetic vortex, locking it into a small region. An abstract concept of the turning vane geometry is shown in Figure 2.

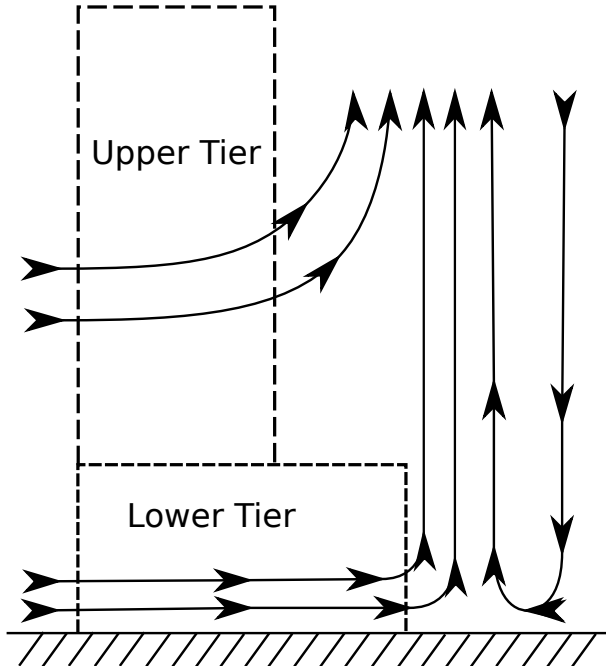


Figure 2: Image of a possible two tier turning vane configuration for generating synthetic dust devils. This image depicts a vertical slice through the proposed configuration, and does not show the reflection of the two tier turning vanes, which would be expected to encircle the dust devil core.

The characteristics of natural dust devils shown in Figure 1 suggest that the turning vanes be structured with two tiers (see Figure 2). The lower tier would be designed to manipulate the surface layer that lifts up into the core of the vortex, while the upper tier would control

entrainment into the vortex. In both tiers, the design of the turning vanes must balance between the need to turn the flow from the radial direction to the azimuthal direction to create vortical motion and the requirement to not block flow into the vortex. Furthermore, in the presence of a cross wind, the vanes need to prevent flow that would pass right through the device, which would disrupt the vortex. Finally, in field tests of design concepts for a solar vortex device conducted by our colleagues at the Georgia Tech, it was found that cross winds over the facility will also disrupt the vortical flow, and that this could be controlled by introducing a conical wind-block on top of the upper tier of vanes. One such field test configuration is shown in Figure 3. Within this broad conceptual design, there remains a large design space to explore, including design parameters for both tiers of vanes and the wind-block cone.



Figure 3: An image of the field configuration from the June, 2015 tests in Arizona. The second (upper) tier of vanes and the cone are clearly visible. This apparatus has an outer diameter of approximately three meters.

To extract energy from the synthetic dust devil formed by the vane system described briefly above, a turbine would be placed near the top of the upper vanes. The turbine would extract energy from both the vertical and azimuthal flow in the vortex, and so the design considerations are different from those for a classical wind turbine. Furthermore, there is presumably an analog to the Betz limit on how much of the energy can be extracted, without disrupting the flow so much that the vortex cannot be maintained. This will need to be explored as part of the turbine design process.

In the research proposed here, the design and performance of a dust devil energy harvesting system will be explored using computational models. Computer models will enable a

more extensive exploration of the design space than would be possible experimentally. The design concept described above will be analyzed to maximize the power that can be generated by the system and to develop scaling describing how power depends on device size, wind speed and thermal conditions. Further new design concepts that may be formulated will also be evaluated. The subsequent section will provide the mathematical representation used to model the system.

### 3 Mathematical Modeling

The aim of the proposed work is to simulate synthetic dust devils in the field. This requires a model of the ambient conditions for a representative case, such as Arizona, where experimental data is available from tests that have been performed. Furthermore, for this to be more generally useful in the prediction of flows in a variety of conditions, we need a model generally applicable to any flow near the surface of the earth.

This section details an analysis of surface fluid mechanics, and develops a mathematical model for turbulence in a thermally stratified medium. We seek to emulate the operation of the apparatus during the day, when dust devils are observed to form readily. At these times, the atmospheric surface layer has the following character. Incident radiation from the Sun does not significantly interact with the air, which is nearly transparent. Instead, this radiation is absorbed by the ground, which causes its temperature to rise. This results in a thermal gradient between the hot ground and the cooler air. The warm ground conducts heat to the air, causing expansion and lowering the density of the air. This reduced density air near the surface is driven upwards by the force of buoyancy.

For sufficiently large temperature gradients, the hot surface layer is unstable, and as the warm air is driven upwards the flow will transition to turbulence. For the typical use case we consider, namely Arizona in summer, the temperature difference can be in excess of 30 Kelvin. Rayleigh numbers associated with temperature gradients of this magnitude are between  $10^9 - 10^{11}$  and therefore meet the criterion for transition to a turbulent regime. The flow is that of an unstably stratified fluid.

This section begins by describing the governing equations of the system of interest. It then proceeds to the development of a viscosity model used to resolve the large scale features of the solution. Next, models used to represent the vanes and turbine, as well as the separation of fluid off of these modeled surfaces, are introduced. Finally, the models for the computational domain extent and the boundary conditions are discussed.

### 3.1 Equations of Fluid Motion

The equations describing fluid flow with natural convection are,

$$\frac{\partial u}{\partial t} + u \cdot \nabla u = -\frac{1}{\rho} \nabla P + \nu \nabla^2 u - g \frac{T'}{T_0} \quad (1)$$

$$\nabla \cdot u = 0 \quad (2)$$

$$\rho c_p \frac{\partial T}{\partial t} + u \cdot \nabla T = \nabla \cdot (k \nabla T) \quad (3)$$

under the assumption that the temperature variation is small in comparison to the mean temperature of the region. These are the incompressible Navier-Stokes equations with Boussinesq, a representation of buoyancy coupled with the heat equation. As discussed above, we anticipate that the flow will be turbulent. Turbulence significantly alters the character of the flow, and necessitates either resolving the resulting small scales or providing a model that emulates their impact. In this case, a Reynolds Averaged Navier-Stokes (RANS) formulation is used, where the turbulent viscosity and thermal conductivities are permitted to vary in space, and the flow is decomposed into constant laminar and varying turbulent and vane components,

$$\begin{aligned} \nu &= \nu_l + \nu_T(z) + \nu_V(r, z) \\ K &= K_l + K_T(z) + K_V(r, z). \end{aligned}$$

This is an effective eddy viscosity model, and the subsequent two sections will elaborate on the spatial dependence and character of  $\nu_T$ ,  $K_T$ ,  $\nu_V$  and  $K_V$ . The laminar, base diffusivities are  $\nu_l$  and  $K_l$ , which do not vary in space.

### 3.2 Viscosity Model

We use the well-known similarity model of Monin and Obukhov[23, 22] as a guide to the specification of an eddy viscosity model to describe the vertical mixing in the atmosphere. This formulation is an extension of the mixing-length model of Prandtl, where the concepts of gradient diffusion and mixing length were generalized to thermally stratified flow.

Monin and Obukhov argued that under statistically stationary, horizontally homogeneous conditions, the dynamics of any mean turbulent quantity ( $\bar{f}$ ) in a thermally stratified medium depend only on,

$$\bar{f} = f(z, \frac{g}{T_0}, \rho_0, \nu_l, K_l, u^*, q). \quad (4)$$

Aside from near the surface, the laminar diffusivities  $\nu_l$  and  $K_l$  will be small compared to their turbulent counterparts,  $\nu_T$  and  $K_T$ , and are therefore negligible. The remaining five parameters are: the distance from the ground,  $z$ ; the buoyancy coefficient,  $\frac{g}{T_0}$ ; the density of the fluid,  $\rho_0$ ; a velocity scale,  $u^*$  (in particular, the freestream velocity); and the heat flux to the ground,  $q$ . These quantities depend on four dimensions: length, time, temperature and mass. Dimensional analysis implies that this mean turbulent quantity ( $\bar{f}$ ) should then only be a function of a single dimensionless group[24]. This is chosen to be,

$$\xi = -\frac{\kappa \frac{g}{T_0} \frac{q}{c_p \rho_0} z}{u^{*3}}. \quad (5)$$

where  $\kappa$  is the (dimensionless) Von-Karman constant. The physical meaning of this quantity bears some discussion. The numerator,  $\kappa \frac{g}{T_0} \frac{q}{c_p \rho_0}$ , is proportional to the buoyant production of kinetic energy. The denominator,  $\frac{u^{*3}}{z}$ , is a shear production rate.

The non-dimensional group  $\xi$  is typically cast into the following form,

$$\xi = \frac{z}{L_{M-O}} \quad (6)$$

where  $L_{M-O}$  is the famous, “Monin-Obukhov” length,

$$L_{M-O} = -\frac{u^{*3}}{\kappa \frac{g}{T_0} \frac{q}{c_p \rho_0}}. \quad (7)$$

This length can be interpreted as the vertical location where the production of buoyantly generated kinetic energy is approximately equal to the energy generated by wind shear. When the magnitude of  $L_{M-O}$  is large, the flow is dominated by shear effects, and the impact of buoyancy is small. Conversely, a small magnitude of  $L_{M-O}$  implies that buoyant effects largely dominate the kinetic energy production. Notice also that the sign convention in Equation 7 is such that for the systems we consider ( $q > 0$ , heat flux from the surface to the air),  $L_{M-O}$  will always be negative. This is as expected, as the convection from the high temperature surface to cooler air is unstable.

In this case, appropriately normalized mean turbulent quantities should be functions of

only the non-dimensional group

$$\frac{\bar{f}}{f_{MO}} = \phi\left(\frac{z}{L_{M-O}}\right) \quad (8)$$

with  $f_{MO}$  a normalizing constant with units of  $\bar{f}$ , and  $\phi$  is a function only of  $\xi$ . We are interested in the case where  $\xi < 0$ , which corresponds to heat flux from the ground into the air. For instance, the mean velocity field would have scaling,  $\frac{u^*}{\kappa}$  and the temperature fields would be scaled as  $T^* = \frac{1}{\kappa u^*} \frac{q}{c_p \rho_0}$ . In this way, the mean velocity and temperature fields would have the form,

$$\bar{u}(z) = \frac{u^*}{\kappa} \phi_u\left(\frac{z}{L_{M-O}}\right) \quad (9)$$

$$\bar{T}(z) = T^* \phi_T\left(\frac{z}{L_{M-O}}\right). \quad (10)$$

As a result, the vertical gradients of the velocity and temperature are necessarily,

$$\frac{\partial \bar{u}(z)}{\partial z} = \frac{u^*}{\kappa L_{M-O}} \varphi_u\left(\frac{z}{L_{M-O}}\right) \quad (11)$$

$$\frac{\partial \bar{T}(z)}{\partial z} = \frac{T^*}{L_{M-O}} \varphi_T\left(\frac{z}{L_{M-O}}\right). \quad (12)$$

Notice that  $\phi$  and  $\varphi$  are different universal functions. Eddy viscosity is defined as,  $u'v' = \nu_T \frac{\partial u}{\partial z}$  [10], in which case, using equation 11, it must scale as

$$\nu_T = \frac{u^{*2}}{\frac{\partial \bar{u}}{\partial z}} = \frac{u^* \kappa L_{M-O}}{\varphi_u(\xi)}. \quad (13)$$

While eddy thermal diffusivity (defined as,  $q = c_p \rho_0 K_T \frac{\partial T}{\partial z}$ ) is

$$K_T = \frac{q/c_p \rho_0}{\frac{\partial \bar{T}}{\partial z}} = \frac{u^* \kappa L_{M-O}}{\varphi_T(\xi)}. \quad (14)$$

Note the difference between  $\varphi_u$  and  $\varphi_T$ , which for turbulent Prandtl numbers near unity (e.g.  $Pr_T \approx 1$ ) the functions will be identical. The asymptotic behavior of the  $\varphi_T$  and  $\varphi_u$  at large and small values of  $\xi$  provides guidance to the more general character of the functions. Our interest lies in the case where  $L_{M-O} < 0$ , which corresponds to heat flux from the ground into the air.

The case where  $\xi \rightarrow -\infty$  implies  $\frac{z}{L_{M-O}} \rightarrow -\infty$  and  $z \gg L_{M-O}$ . This is most readily interpreted as the instance where  $u^* \rightarrow 0$ , e.g. the buoyancy-dominated case with no wind

(free-convection). For this case, the function  $\varphi_T$  must have no dependence on  $u^*$ , and will approach a constant. Scaling analysis implies that the overall function will not depend on  $u^*$  only when the function  $\varphi$  scales to the  $-\frac{4}{3}$  power. The function must then be

$$K_T = \frac{1}{C_T} \left( \frac{q}{c_p \rho_0} \frac{g}{T_0} \right)^{\frac{1}{3}} z^{\frac{4}{3}} \text{ for } z \gg L_{M-O}. \quad (15)$$

So long as the Prandtl number remains constant in space, then identical arguments regarding the asymptotic behaviour at large  $\xi$  provide the analogous result for the eddy viscosity's variation with respect to distance from the ground,

$$\nu_T = \frac{1}{C_{\nu_T}} \left( \frac{q}{c_p \rho_0} \frac{g}{T_0} \right)^{\frac{1}{3}} z^{\frac{4}{3}} \text{ for } z \gg L_{M-O}. \quad (16)$$

These functions have been found to be broadly applicable and accurate[12], and are easily implemented in software.

### 3.3 Eddy Viscosity in the Device

The validation process identified a refinement to the virtual vane formulation that results in a better representation of the vane effects in a broader range of flows. The thermal and momentum diffusivities are even larger in the device where the flow across the vanes produces shear and generates turbulence. The model now include an enhanced turbulent diffusivity in the vortical plume region to account for the effects of vortex shedding from the trailing edge of the vanes, which is not represented in the virtual vane representation (discussed in 3.4).

The eddy-viscosity in the region of the vanes and interior is set based on scaling relations for a turbulent self-similar circular jet, as described in Pope[26],

$$\nu_C = U_0 y_{1/2} \bar{\nu}_C. \quad (17)$$

In this equation,  $U_0$  is the peak velocity, and  $y_{1/2}$  the jet half-width (taken to be the dust devil half-width). The dimensionless constant  $\bar{\nu}_C$  is calibrated based on experimental data, and is set to zero outside the device. The thermal diffusivity inside the device,  $K_C$ , is then fixed with the assumption that the Prandtl number is unity.

### 3.4 Vane and Turbine Representation

To rapidly prototype general system configurations, the computations must be able to explore a large space of possible geometries and settings. This presents a significant meshing and computational challenge if the detailed flow around the vanes is to be computed. In the region near the vanes, where a no-slip boundary condition is imposed, the flow will necessarily form a thin momentum boundary layer. Resolving this boundary layer requires high resolutions immediately adjacent to the walls. Changing the vane location requires that a new mesh be generated. This is a significant challenge, as the development of a new mesh often requires significant human effort and time. Furthermore, the process is error-prone, and would require that each simulation using a new mesh undergo detailed solution verification.

Instead, we have developed a modeling formulation that does not require explicitly meshing the turning vanes, or any surface. These so-called “virtual vanes” are implemented as a body force that is applied in the annular region that contains the vanes. Vane geometry is specified by the angle  $\phi$  a vane makes with a radial line as a function of the radial coordinate  $r$ . A unit normal to vane surfaces  $\mathbf{n}$  is defined as

$$\mathbf{n}(\mathbf{x}) = \sin(\phi(r)) \hat{\mathbf{r}} + \cos(\phi(r)) \hat{\theta} \quad (18)$$

where  $\hat{\mathbf{r}}$  and  $\hat{\theta}$  are unit vectors in the radial and azimuthal directions, respectively. With this vane-normal vector field specified, a body force  $\mathbf{f}_v$  is defined that will drive the velocity in the  $\mathbf{n}$  direction toward zero, effectively turning the flow to be parallel to the vanes. The body force is defined:

$$\mathbf{f}_v = -\frac{1}{\ell_v} |\mathbf{u}| (\mathbf{u} \cdot \mathbf{n}) \mathbf{n} \quad (19)$$

with  $\mathbf{u}$  the velocity and  $\ell_v$  is a specified length scale.  $\ell_v$  represents the distance over which the flow evolves under the influence of the body force before the velocity in the normal direction is reduced by a factor of  $1/e$ . In other words, this is the length scale over which the normal component of the velocity decays exponentially. It is a modeling constant and is specified to be the same order as the separation distance between neighboring vanes in the physical vane configuration, since entry lengths in internal flows scale with the width of the channel.

This virtual vane formulation is similar to the “actuator disk” model commonly used to represent the rotor of a wind turbine [32]. An actuator disk model is under development and will be detailed in the dissertation.

### 3.5 Solid Surface Representation

In addition to vanes, the SoV device includes impermeable surfaces such as the wind break (“cone”) on the top of the facility. As with the turning vanes, this is represented without explicitly meshing the surface nor imposing a boundary condition at the surface. This allows rapid exploration of configurations with different solid surfaces to control and manipulate the fluid flow. These solid surfaces are represented by a body force acting in a region surrounding the wall. A body force normal to the surface is defined in this region so that it will drive the normal velocity to zero, resulting in the flow moving only parallel to the virtual surface. The body force is defined as in Equation 19; however, the length scale  $\ell_v$  is specified to be identical to the width of the surface being represented. This is typically the width of two or three grid cells. While the actual surface we are emulating is thinner than this, the numerical method has difficulty converging for surfaces smaller than the grid size.

Forcing models designed to mimic a surface are not unique to this project, and the current formulation is closely related to (among others) “immersed boundary methods” as used by various other researchers[20]. This approach is unique in its use of Babuska’s penalty treatment of constraints[2, 30] to enforce the behavior at the boundary. This method was selected because it is easily imposed in the FEM context, and the method has been explored in detail in the literature.

### 3.6 Separation Model

In the presence of wind, it was found that there was a significant flow out through the vanes in the back of the device. This was obviously inconsistent with the findings of our colleagues in the field, who observed no outflows out of the back of the device. Moreover, this resulted in large inconsistencies between our predictions and the field results, almost certainly because of the kinetic and thermal energy that our vane representation was permitting to leave out the back of the device.

This exposed a weakness of the turning vane representation outlined previously. When the flow entered the virtual vane forcing region it was always turned to align with the vane angle, even when the forcing was in the opposite direction of the present velocity. This is in contrast to the physical situation, in which we expect the flow to continue along an averaged streamline separating from the trailing edges of the vanes, instead of turning around it. The averaged streamline will continue past the trailing edge of the vane due to the separation of the boundary layer off the edge surface. An image depicting these two cases is shown in

Figure 4.

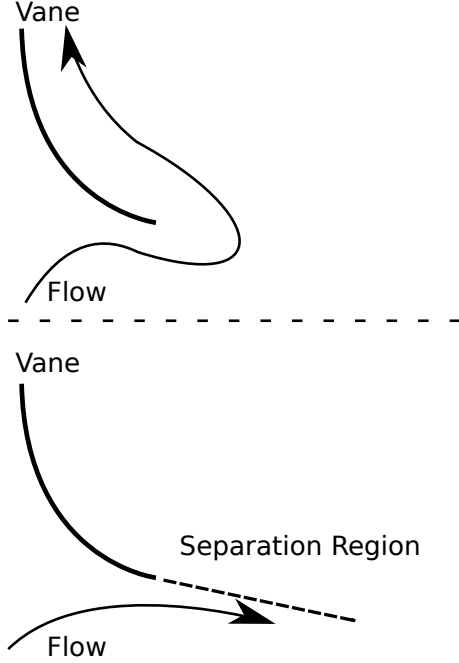


Figure 4: Schematic depicting the separation model that extends past the trailing edge of the vanes. In the top case, the flow entering the virtual vane region is forced to align with the vane angle despite this resulting in a reversal of the flow direction. This is a consequence of the forcing function acting on the fluid to ensure the velocity vector aligns with the vane. The second case depicts the separation model, where the flow under certain conditions is not forced and continues to move tangent to the vanes due to the separation of the boundary layer off the trailing edge.

Let  $\mathbf{n}^v$  be the normal vector to the vanes, and  $\mathbf{n}^r$  the normal vector pointing out of the vane region<sup>2</sup>. Then,  $\mathbf{t}^v$  is the tangential vector to the vanes pointing out of the vane region and is defined as,

$$\mathbf{t}^v = \left( \mathbf{n}^{v\perp} \right) \text{sign} \left( \mathbf{n}^{v\perp} \cdot \mathbf{n}^r \right). \quad (20)$$

Here,  $\mathbf{n}^{v\perp}$  is the vector perpendicular to the normal vector of the vanes, which is simply,

$$\mathbf{n}^{v\perp} = \begin{bmatrix} n_x \\ n_y \end{bmatrix}^\perp = \begin{bmatrix} -n_y \\ n_x \end{bmatrix}.$$

---

<sup>2</sup>The superscripts “v” and “r” stand for vane and radial, respectively.

---

**Algorithm 1** The crude separation model. This model identifies if the flow is coming into or out of the vane region, and if the velocity vector is in the same direction as the tangent line of the vanes. In the case of the “special forcing” the flow is forced as if it was impacting a solid surface. In the algorithm below,  $r_0$  is the max radius of vanes,  $r_i$  the minimum radius of vanes, and  $\delta$  is the width of the separation region.

---

```

1: if ( $r_0 > r > r_i$ ) then
2:   if ( $r_0 - r < \delta$  or ( $(r - r_i) < \delta$ ) then
3:      $\vec{n}^r = \vec{r}/|r|$ 
4:     if ( $r - r_i < \delta$ ) then
5:        $\vec{n}^r = -\vec{n}^r$ 
6:     end if
7:      $\mathbf{t}^v = (\mathbf{n}^{v^\perp}) \text{sign}(\mathbf{n}^{v^\perp} \cdot \mathbf{n}^r)$ 
8:     if  $v \cdot t^v > 0$  and  $v \cdot n^r < 0$  then
9:        $\mathbf{n}(\mathbf{x}) = \hat{r}$     (Special Forcing)
10:    else
11:       $\mathbf{n}(\mathbf{x}) = \sin(\phi(r)) \hat{\mathbf{r}} + \cos(\phi(r)) \hat{\theta}$     (Normal Forcing)
12:    end if
13:  else
14:     $\mathbf{n}(\mathbf{x}) = \sin(\phi(r)) \hat{\mathbf{r}} + \cos(\phi(r)) \hat{\theta}$     (Normal Forcing)
15:  end if
16: end if
```

---

The forcing is modified when the velocity vector of the local flow,  $\mathbf{u}$  is pointing in to the forcing region:  $\mathbf{u} \cdot \mathbf{n}^r < 0$ , and when the velocity vector is in the same direction as the tangent line to the vanes:  $\mathbf{u} \cdot \mathbf{t}^v > 0$ . In these instances, the forcing acts as if there was a rigid surface past the vane edge, and gives the appearance of a special “no-penetration” condition for the velocity for these cases. The pseudo-code for this procedure is shown in Algorithm 1.

The addition of this simple separation model significantly reduced the flow that penetrated the back of the vanes, and produces results consistent with the observations provided by our experimental colleagues.

### 3.7 Effect of Surface Roughness

Surface roughness effects have been shown to play a role in the formation of dust devils and related atmospheric phenomena[25]. For the flat and sandy regions we are simulating, the impact is expected to be a small velocity perturbation in the vertical direction. This is modeled as a volumetric forcing in a narrow region above the surface,

$$F_{z_0}''' = \frac{1}{2}\rho V_z^2/z_0, \quad (21)$$

where  $z_0$  is the roughness height. We ensure that the energy introduced into the flow is a small fraction of total flow energy by comparing this with the energy flux through the top of the vanes. The total energy added is measured as,

$$E_{\text{injected}} = \int_0^{2\pi} \int_0^R \int_0^{z_0} F_{z_0}''' dz dr d\theta. \quad (22)$$

$R$  is the outer diameter of the vanes. The value of  $E_{\text{injected}}$  is typically a few percent of the total kinetic energy flux measured through the top of the vanes.

### 3.8 Simulation Geometry and Boundary Conditions

In this project, two principle modeling regimes are considered. One is the “thermal-only” scenario, in which there are no ambient velocities and there is an imposed elevated temperature on the ground. In the other, there are also ambient winds that contribute to the SoV energy (“wind” cases). The computational domain and boundary conditions for these two scenarios are described below.

## Computational Domain

All simulations are performed in a cuboid domain, with six faces. The domain is denoted  $\Omega \subset \mathbb{R}^3$ . The domain extents are scaled by the system diameter,  $D$ , created by the outer vane radius. The extents are defined in terms of  $\{L_x, L_y, L_z\}$  indicating the streamwise, spanwise and vertical directions, respectively. For both simulation regimes, sensitivity analyses were performed to ensure that the results were not sensitive to the domain extents. For the thermal-only case, for which  $L_x = L_y$ , the system extents  $L_x/D$  and  $L_y/D$  are chosen to be 3. The height ( $L_z/D$ ) is three times the system diameter, which is typically nearly equal to the height of the vanes. This defines the thermal-only domain  $\Omega_T$ , as  $\Omega_T = [-L_x, L_x] \times [-L_y, L_y] \times [0, L_z]$ .

For the wind cases, the streamwise extent is no longer equal to the spanwise length,  $L_y$ . In these cases, the domain length extends two diameters in front of the vanes and three behind. The spanwise direction is symmetric and extends two diameters in each direction from the center ( $L_y/D = 2$ ). The height is identical to the thermal-only case, at three system diameters ( $L_z/D = 3$ ). Thus, the wind domain is defined as  $\Omega_W = [-2D, 3D] \times [-L_y, L_y] \times [0, L_z]$ .

The boundary for the thermal only case is decomposed as,  $\partial\Omega_T = \Gamma_G \cup \Gamma_T \cup \Gamma_P$ .  $\Gamma_G$  is the boundary along the “Ground”,  $\Gamma_T$  the “Top” boundary, and  $\Gamma_P$  the four periodic “Sides”. A 3d diagram labeling these boundaries is shown in Figure 5. For this case study (no mean wind), periodic boundary conditions are used on the four sides , with a modified “inflow-outflow” Neumann condition[13] on the top boundary. On the ground, a “no-slip” velocity boundary condition is imposed, and a Dirichlet condition uniformly fixes the temperature of the surface. Each of the  $\Gamma$  boundary terms are defined in the paragraphs below. Note that a finite thickness “Sponge Layer” is indicated on the figure along the top boundary and is defined below.

The boundary for the wind cases is decomposed as,  $\partial\Omega_W = \Gamma_G \cup \Gamma_T \cup \Gamma_O \cup \Gamma_I \cup \Gamma_S$ . Where  $\Gamma_G$  is the boundary along the “Ground”,  $\Gamma_T$  the “Top” boundary,  $\Gamma_S$  the two “Sides”,  $\Gamma_I$  the inflow boundary, and  $\Gamma_O$  the “Outflow” boundary. The “wind” simulation domain is diagrammed in Figure 6, with the boundaries labeled. For this particular study (a heated ground with an ambient wind), the wind case has a proscribed inlet boundary layer along the upstream streamwise face ( $\Gamma_I$ ) for both the temperature and the velocity. The “Ground” boundary is identical to the thermal-only case. The “Sides”, “Outflow” and “Top” are all set to modified Neumann boundary conditions. Note that “Sponge Layers” are used on both the back boundary and the top.

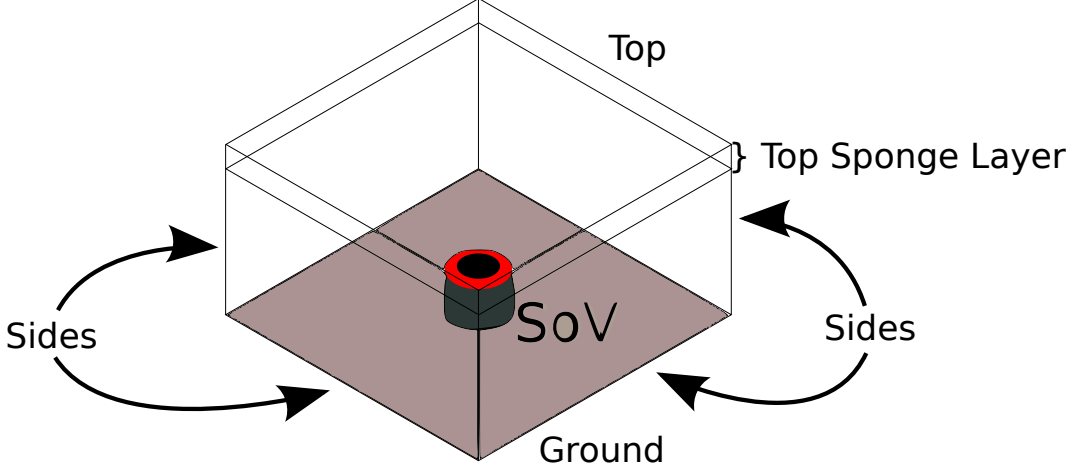


Figure 5: Domain for the thermal-only scenario. The diagram scale is representative of typical cases. Note the SoV apparatus in the center, which provides perspective on the extent of the domain with respect to the turning vane diameter. The ground, sides and top boundaries are labeled with the discussion the precise boundary conditions on each provided in section 3.8. Notice also the finite thickness, high viscosity “sponge layer” at the top of the domain.

### Ground Boundary Conditions, $\Gamma_G$

For both the wind and thermal-only cases the ground has a fixed temperature and no-slip velocity boundary conditions. This boundary ( $\Gamma_G$ ) is modeled with a Dirichlet boundary condition,

$$\vec{u} = 0 \quad \text{on } \Gamma_G \quad (23)$$

$$T = T_g. \quad (24)$$

Where  $\Gamma_G = \{(x, y, 0) \subset \partial\Omega\}$ .

### Periodic Boundary Condition, $\Gamma_P$

A periodic boundary condition is used in the thermal only cases, along the streamwise and spanwise boundary faces (denoted  $\Gamma_{P,x}$  and  $\Gamma_{P,y}$ , respectively). In these cases the state variables are constrained to have the same value on the opposite faces of the domain, for instance in the streamwise direction the boundary conditions are,

$$\vec{u}(-L_x, y, z) = \vec{u}(L_x, y, z) \quad \text{on } \Gamma_{P,x} \quad (25)$$

$$T(-L_x, y, z) = T(L_x, y, z) \quad (26)$$

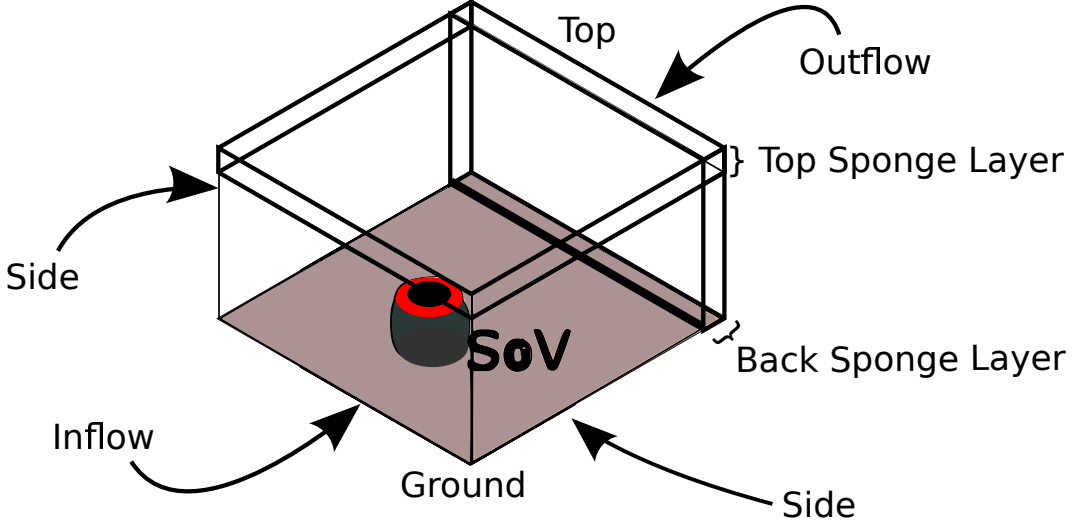


Figure 6: Domain for the wind and thermal scenario. The diagram scale is representative of typical cases. Note the SoV apparatus which provides perspective on the extent of the domain with respect to the turning vane diameter. The ground, sides, inflow, back and top boundaries are labeled with the discussion the precise boundary conditions on each provided in section 3.8. Notice also the finite thickness, high viscosity “sponge layer” at the top and back of the domain.

and in the spanwise direction,

$$\vec{u}(x, -L_y, z) = \vec{u}(x, L_y, z) \quad \text{on } \Gamma_{P,y} \quad (27)$$

$$T(x, -L_y, z) = T(x, L_y, z). \quad (28)$$

Where  $\Gamma_{P,x} = \{(-L_x, y, z) \cup (L_x, y, z) \subset \partial\Omega\}$  and  $\Gamma_{P,y} = \{(x, -L_y, z) \cup (x, L_y, z) \subset \partial\Omega\}$ .

#### Inflow Boundary Condition, $\Gamma_I$

On the inflow boundary ( $\Gamma_I$ ), dirichlet conditions are used for both velocity and temperature. The boundary-normal, or streamwise component is a function of the surface normal coordinate ( $z$ ), representing a boundary layer below a uniform velocity,  $U$ . The common 7th power model of a turbulent boundary layer is used,

$$u_{in}(z) = U \min \left( \left( \frac{z}{\delta} \right)^7, 1 \right)$$

where  $\delta$ , the boundary layer thickness, is set based on data measured by our experimental partners in the field. The thermal boundary layer is assumed to have a similar boundary

layer, but, as observed in real atmospheric flows, there remains a vertical temperature gradient outside the thin boundary layer. Based on results in the literature a 2/3 Kelvin per meter gradient is imposed[6]. The thermal inflow is then

$$T_{\text{in}}(z) = \Delta T \left( 1 - \min \left( \left( \frac{z}{\delta} \right)^7, 1 \right) \right) + T_0 - 2z/3.$$

The inflow boundary is at the surface  $x = -L_x$ .

### Mixed inflow/outflow Boundary Conditions on $\Gamma_T$ , $\Gamma_S$ and $\Gamma_B$

At outflow boundaries, a homogeneous Neumann condition is appropriate,

$$\frac{\partial u}{\partial n} \Big|_{\Gamma_T} = 0 \quad (29)$$

$$\frac{\partial T}{\partial n} \Big|_{\Gamma_T} = 0 \quad (30)$$

However, for the cases in this study, a modified Neumann condition is necessary due to the possibility that there will be an inflow on these boundaries. For example, in the region above the vanes, the concentrated hot plume is lifted by buoyancy upward and out of the simulation domain. However, the radial inflow towards the apparatus is drawn in by large scale convection cells larger than the system diameter. Thus, our boundary conditions must permit inflow along the areas above and external to the vanes, while simultaneously permitting outflow in the area above the vanes.

To accomplish this, the boundary condition is,

$$\frac{\partial u_n}{\partial n} \Big|_{\Gamma_T} = 0 \quad (31)$$

$$\text{if } (w < 0) \text{ then } \begin{cases} u_t = 0, \\ T = T_{\text{in}} \end{cases} \quad (32)$$

$$\text{else } \begin{cases} \frac{\partial u_t}{\partial n} \Big|_{\Gamma_T} = 0, \\ \frac{\partial T}{\partial n} \Big|_{\Gamma_T} = 0 \end{cases} \quad (33)$$

where  $u_n$  and  $u_t$  are normal and tangential components of the velocity, respectively. This boundary condition is applied on the top boundary  $\Gamma_T$  ( $z = L_z$ ) and downstream side boundary  $\Gamma_B$  in the wind case.

### Sponge Layer

Finally, a finite thickness “sponge layer” is used in the region adjacent to the mixed inflow/outflow boundaries  $\Gamma_T$  and  $\Gamma_B$ . This layer artificially increases the momentum diffusivity by up to a factor of ten times the nominal value. This was designed to stabilize the modified Neumann boundary conditions which can exhibit an instability when there is a compact jet of fluid leaving the domain. These regions are referred to by many names in the literature[9], such as absorbing layers, fringe regions, buffer zones, sponges, etc.

## 4 Computational Methods and Software

The previous section described a series of models for the system of interest. This section details the numerical formulation and simulation of these models. It begins with a discussion of the numerical discretization of the equations of interest. The mesh discretization is then described. Next, the scientific software in which these numerical models are used is discussed. Finally, the tool chain and supercomputer systems are briefly introduced.

### 4.1 Discretization Scheme

To numerically solve the Navier-Stokes equations on a computer, a Galerkin finite element method (FEM) is used, which requires that the equations in section 3.1 be cast into a weak form. Manipulating these partial differential equations into a variational formulation is accomplished by multiplying the equations by appropriate test functions and integrating over the domain,  $\Omega$ . The resulting weak problem is to find,  $(u, p, T) \in H^1(\Omega)^3 \times L_2(\Omega) \times H^1(\Omega)$  such that

$$\left( \frac{\partial u}{\partial t}, v \right) + (u \cdot \nabla u, v) + \nu (\nabla u, \nabla v) - (p, \nabla \cdot u) = (gT'/T_0, v) \quad (34)$$

$$(\nabla \cdot u, q) = 0 \quad (35)$$

$$\left( \frac{\partial T}{\partial t}, w \right) + (u \cdot \nabla T, w) + (k \nabla T, \nabla w) = 0. \quad (36)$$

$\forall (v, q, w) \in H^1(\Omega)^3 \times L_2(\Omega) \times H^1(\Omega)$ , where  $(u, v) = \int_{\Omega} u \cdot v \, dx$ . Some of the simulations presented here were conducted under steady conditions, for which the  $\frac{\partial}{\partial t}$  terms vanish. A Galerkin FEM scheme is obtained by posing the weak form in terms of discrete subspaces of the function spaces specified above defined using piecewise-polynomial basis functions. All of the simulations discussed in this work were accomplished using linear basis functions for both the velocity and pressure. The scheme is stable with equal-order elements for velocity and pressure due to the introduction of streamline upwind/Petrov-Galerkin (SUPG) stabilization terms as first described by Hughes[15, 8] and extended to natural convection as in Becker and Braack[5]. The stabilization terms add artificial dissipation that approaches zero as the residual converges. This scheme is “consistent” because the underlying order of convergence of the numerical method is not affected[16].

This stabilization is accomplished by introducing an additional term,  $\langle Lc, S\phi \rangle_{\tau}$ , to the weak form defined in Equations 34–36. Here  $L()$  is the operator for the PDEs in 3.1,  $S$  is a

stabilization operator which is chosen to be the negative adjoint of the differential terms of  $L()$ , and  $c$  and  $\phi$  are state and test functions, i.e.  $c = (u, p, T)$ , and  $\phi = (v, w, q)$ . The angle brackets  $\langle \cdot, \cdot \rangle$  signify integration of the element interiors for each of the  $K$  elements, that is:

$$\langle u, v \rangle_{\tau} = \sum_K \tau_K(u, v)_K. \quad (37)$$

This results in three stabilization parameters,  $\tau_P, \tau_v, \tau_T$  which are selected as proposed by Becker and Braack. A full derivation of the weak form and stabilization terms will be provided in an appendix of the full thesis.

The system of ODEs are discretized in time using the backward Euler method[21]. The time interval  $(0, T)$  is sliced into  $N_t$  steps of uniform temporal length,  $\Delta t$ , where  $n = 0, \dots, N_t$ . This has the form,

$$y_{n+1} = y_n + \Delta t f(y_{n+1}, t_{n+1}). \quad (38)$$

As  $f$  is non-linear, a Newton-Raphson method is used to solve the resulting implicit nonlinear problem. While an iterative method is significantly more computationally expensive per timestep than a similar explicit method, the method was selected due to its unconditional stability and ease of statistical sampling for a uniform timestep.

## 4.2 Mesh Discretization

The domain's described in subsection 3.8 are consistently discretized. The domain extents are scaled by system diameter but the same number of grid points are used for every simulation. Thus, while the ratio of the domain length to system diameter remains fixed, the grid spacing increases proportionally with domain length.

The mesh has a uniform spacing in the lateral directions, except for a single refinement in the region of the vanes. Typically, the grid is roughly one hundred points in the streamwise and spanwise directions before the refinement. The refinement halves the spacing (doubles the number of points) in all three coordinate directions, {x,y,z} in this region. The refinement is made from the ground to 1.5 times the height of the vanes and cone.

The mesh is non-uniform in height to resolve the boundary layer. This is accomplished

by redistributing a mesh uniform in height,  $z$ , according to,

$$z = \begin{cases} C_1(z - L_z) + L_z, & \text{if } z \geq z_\delta \\ C_2 \exp(C_3 z - 1), & \text{otherwise} \end{cases} \quad (39)$$

where  $z_\delta$  is the chosen height of the boundary layer mesh, and  $C_1 - C_3$  are scaling coefficients. This gives the mesh an exponentially varying character, with the coefficients chosen to ensure ten or more points in the boundary layer, isotropic spacing in cells outside of it, and smooth blending between these two regimes. Each boundary layer spacing was tested against a finer spacing to ensure that the results were not sensitive to the choice of spacing. A horizontal slice through a representative domain is shown in Figure 7. The single refinement in the region of the vanes is visible, as well as the finer meshed boundary layer region near the ground.

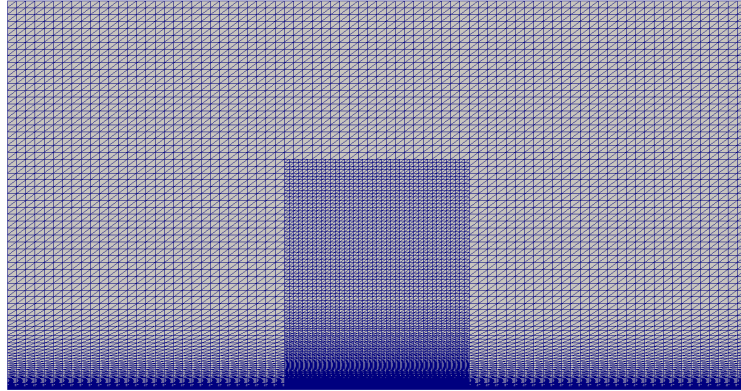


Figure 7: Horizontal slice through the domain, to show a representative meshing. The single refinement region around the vanes is visible, as well as the finer boundary layer mesh near the ground.

Finally, the diffusivities are proportionally scaled with grid size to ensure that the cell Reynolds number,

$$\text{Re}_{\text{cell}} = \frac{\max(\Delta x, \Delta y) u}{\nu_T} \quad (40)$$

is maintained for every simulation, in order to ensure stability.

### 4.3 Software Stack

The numerical approximations described above had been implemented using the GRINS library[4] by Bauman and Stogner using the Libmesh[18] FEM infrastructure. It was designed to support multiphysics FEM applications, the reusability and extensibility of mathematical modeling kernels, supporting interfaces to existing solver and discretization libraries to enable modern solution strategies, while, at the same time, retaining flexibility to effectively address a wide range of science or engineering problems.

GRINS provides a platform that enables powerful numerical algorithms such as adjoint-based AMR, adaptive modeling, sensitivity analysis, and, eventually, enabling uncertainty quantification. While few of these capabilities are in use for the present work, they could be useful in future investigations.

GRINS stands for, “General Reacting Incompressible Navier-Stokes”, which roughly encapsulates the physical regimes it was originally designed to simulate. GRINS is open-source, and available on github. It is released under LGPL2.1. GRINS is heavily unit tested, with over 60 tests available to ensure the reliability of results regardless of install platform.

### 4.4 Tool Chain and Simulation Custodianship

Simulations are performed on the Texas Advanced Computing Center (TACC) supercomputers Lonestar Four and Stampede. Run durations for transient cases are typically twelve hours to perform several hundred timesteps. These runs are submitted to the production queue and are 264-528 processing cores, or 22-44 nodes on Lonestar (with 12 cores per node), and a similar number for Stampede. The runs typically have several million degrees of freedom (DoF), and the local number of DoF per core is maintained at  $O(10^4)$ . This was selected due to memory constraints, after a strong scaling analysis of the performance of the code on these resources, and after consulting with the software developers.

After a run terminates, several scripts are automatically invoked. These scripts archive the run (outside of the volatile /scratch production directories) and simultaneously, label the concluded run with unique metadata that defines the system environment, the jobs input files and run definitions, as well as information detailing the hypothesis or physics the job was intended to investigate. Finally, once a week a script performs **rsync** on the entire archived database to ensure more than single redundancy for the runs.

In other words, the workflow is designed to permit rapid queuing of a series of runs (in parallel) to investigate a variety of conditions or scenario parameters. This capability

is necessary for the optimization campaign detailed in 7, where running many concurrent investigations will be required to adequately sample the configuration space.

## 5 Validation

The previous sections briefly outlined the physical phenomenon under consideration, the mathematical models proposed to simulate it, and the numerical solution of these models for a variety of system configurations and scenarios. Before these simulations can be used as a tool to evaluate proposed system designs, it is necessary to validate that the physical model in use accurately represent reality. This section contains a discussion of the validation of the computational models against existing experimental data and high fidelity simulations.

A challenge in this project is the scarcity of experimental data. Only two or three cases of experimental measurements are available. These measurements, for reasons detailed in the next subsection, are not sufficient to provide confidence in the output of simulations across a wide variety of scenarios. Therefore, a high fidelity model using meshed vanes with enforced no-slip velocity boundary conditions along the surface of the vane was developed. These “gridded” runs have been validated against the experimental data, which they match quite closely. However, as detailed in Section 3.4, explicitly meshing the vanes would be far too prohibitively expensive to permit a rapid exploration of a variety of system configurations. Instead, this high fidelity model is used to generate additional reliable data to permit validation of lower fidelity models, such as the virtual vanes. Likewise, the results of the unsteady virtual vane simulations can be used as validation data for a further reduced, steady Navier-Stokes model. This hierarchy of validation is shown in Figure 8, with data sources that generate more reliable data at the top, and models that are less reliable, but also less computationally expensive at the bottom. In terms of expense, the steady virtual vane model generates a solution in approximately two minutes, versus twelve hours for the unsteady virtual vane model. The gridded vanes require another factor of ten in computational time, and many more man-hours hours of work to generate the mesh. Therefore, it is unrealistic to perform parameter sweeps or system configuration investigations with the gridded vanes and these results are used only for validation studies. Instead, the ROM is used, with promising results re-evaluated with unsteady virtual vane models.

Three kinds of experimental validation data are available. These are data generated in the laboratory using a heated plate, data from experiments in the wind tunnel (“Wind-only”), and measurements from field tests (“Field”) conducted in Arizona. The available data from these cases as well as the gridded vanes created to mimic them are summarized in Table 1. Every case shown has been simulated using the virtual vanes.

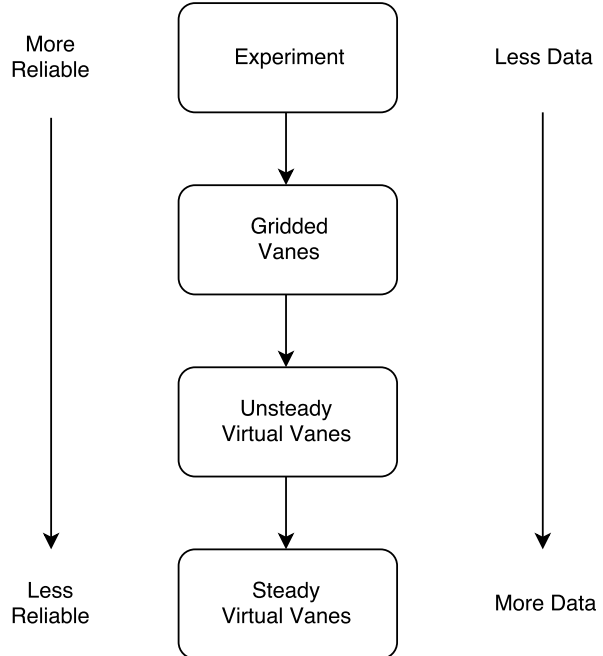


Figure 8: This figure depicts the validation hierarchy. The experimental measurements are at the top, where the data is expected to be the most reliable, but simultaneously the most limited. Moving down the table leads to simulated data sources that are less reliable but increasingly cheaper in time to generate. At the bottom is the reduced order model from steady virtual vane solutions.

## 5.1 Thermal-Only Validation

This section provides examples of the validation performed with the richest data set, the measurements in the laboratory. All of the thermal-only data was generated in a laboratory setting at Georgia Tech. The general system configuration is depicted in Figure 9. These data were taken using particle image velocimetry (PIV), and the errors in measurement and sampling are not known. In addition, only velocity measurements are available. Several potentially important quantities of interest, such as the pressure and temperature, have not been measured.

While no sensitivity analysis has been performed, it is likely that the largest uncertainty in the laboratory simulation is a result of the ventilation of the laboratory. The heated plate at the bottom of the apparatus generates enough heat to cause a significant increase in room temperature (30+ Kelvin), which greatly impacts the SoV performance, as the ground to air thermal gradient drives the vortex. The laboratory is cooled to maintain temperature by two inlet HVAC ducts into the room. One vent continuously provides air at 288 Kelvin with

	Wind-Only	Thermal-Only	Field
Experiment	Straight Vanes 60°	Straight Vanes 60° Straight Vanes 30° Hybrid (Two tier)	June 2014 August 2014 August 2015
Gridded	Straight Vanes 60° Straight Vanes 30°	Straight Vanes 60° Straight Vanes 30°	

Table 1: Available truth data from the laboratory experiments (cold wind and thermal-only), the field test, and the gridded vanes.

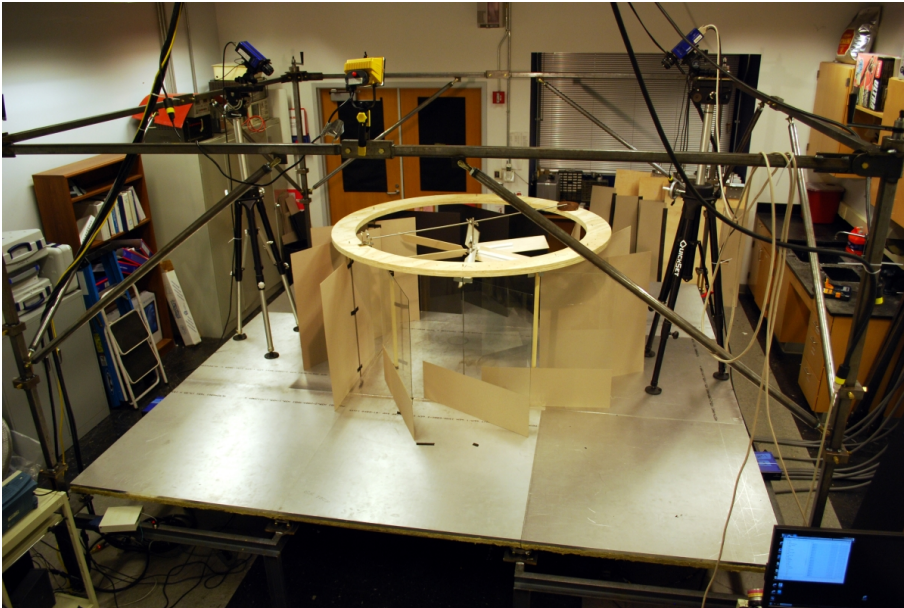


Figure 9: The single tier straight vane laboratory configuration. The apparatus is shown with a turbine, but that was removed for data gathering.

a flow rate estimated to be  $1 \text{ m}^3/\text{s}$ . The other vent is active only if the room temperature exceeds 301 Kelvin, with a flow rate also estimated at  $1 \text{ m}^3/\text{s}$ . Finally, the air leaves through the cracks around the laboratory doors and exhaust vents. Preliminary results indicated that an inflow rate of  $1 \text{ m}^3/\text{s}$ , the lower bound of the possible inflow rates results in excessive heating of the room, while inflow conditions at the maximum inflow rate of  $2 \text{ m}^3/\text{s}$  result in a simulated room that is too cold, compared to the laboratory.

Our simulated vortices are sensitive to ambient room temperature and thus the inflow rate. It is likely that the laboratory is run where one of the vents is operating intermittently. To mimic these conditions in our simulations, Dirichlet boundary conditions on parts of the sides of the computational domain are used to establish a constant inflow of cool air at

the rates proscribed by our collaborators. Over the remainder of the side walls, adiabatic thermal boundary conditions are used.

The most significant boundary condition disparity is that flow leaves the domain through the top boundary, instead of out of the sides of the room. Preliminary results suggested that the SoV phenomenon was not sensitive to these boundary condition details. The important element is the global energy balance in the room. The flow rate into the room is adjusted to  $1.3 \text{ m}^3/\text{s}$  for the validation results discussed here.

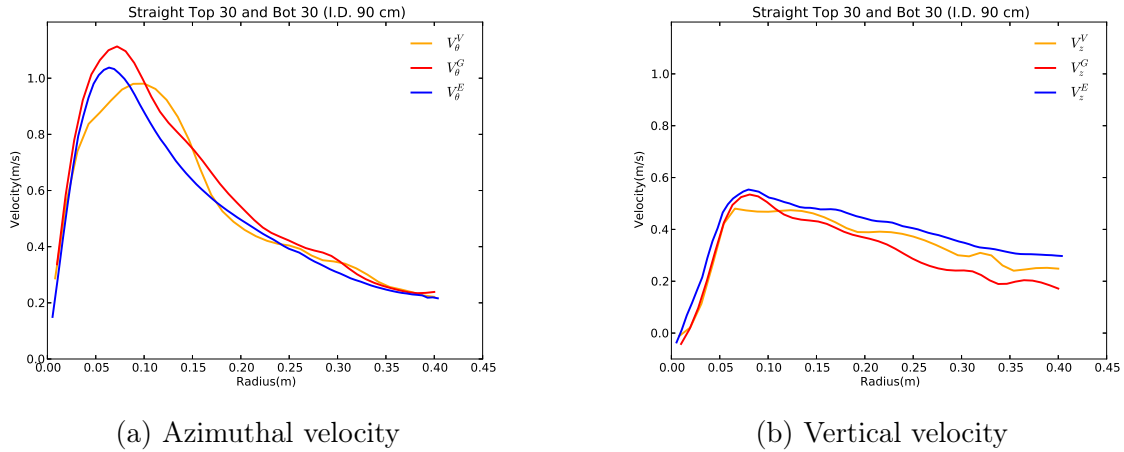


Figure 10: Azimuthal (left) and vertical (right) velocity as a function of radius for the thermal-only cases. The gold line is the virtual vane simulation, blue the experiment, and red the gridded vane.

Figure 10 is a direct comparison between laboratory measurements for a simple single tier vane configuration ( $30^\circ$  straight vanes) and nominally identical simulations with the gridded and virtual vanes. The simulations and experiment broadly agree. The simulation correctly reproduce the peak structure in the azimuthal velocity observed for this configuration in the experiment. The gridded vanes closely represent the peaks radial location, while the virtual vanes over-predict the radial location. The radial location of peak vertical velocity also closely agrees with experiment.

Similar validation comparisons have been made between several other configurations with similar levels of agreement, notably the  $60^\circ$  single tier straight vane case, and the two tier hybrid vane. Finally, estimates of the energy fluxes between the field configuration and our simulation results agreed within 15%. These validation studies have provided a level of confidence that our simulations accurately reproduce the phenomena observed in laboratory.

## 5.2 Wind Cases

The laboratory thermal vortex experiments described in the previous subsection did not include the effects of the wind, but experience in the field indicated how important these effects were. To ensure that the virtual vanes could represent this effect, a validation study was performed using the data obtained in the wind tunnel.

A numerical experiment was performed in which the 60 degree single tier straight vanes were placed in a isothermal wind. These results were compared to an identical configuration placed in a wind tunnel. However, no measurements (of velocity or any quantity) were made for the vanes in these conditions. Qualitative comparisons, based on descriptions of observed structures and videos of smoke visualization were made between the simulations and the wind tunnel experiments. These images and discussions did not identify any inconsistencies between simulation and experiment. However, these results are limited, and are only for the cold wind, as the wind tunnel did not include a heated plate.

Figure 11 contains images of the simulated averaged streamwise and spanwise velocity in a horizontal plane at approximately the height of the vanes obtained from simulations with gridded and virtual vanes. As expected, there are some differences in the details of these simulations, but the overall character of the flow inside the vanes, and in the wake of the vanes is quite similar. This demonstrates that the virtual vane formulation can indeed represent the interaction with the wind.

## 5.3 Field Configurations

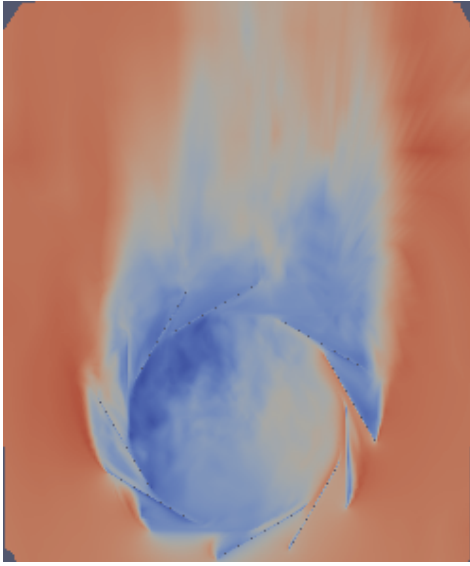
Several field tests have been performed by the experimental team. After each field test, qualitative observations, measurements and lessons learned are provided by the field team. Actual measurements are limited. Due to the complexity of the configuration (two vane tiers and a cone) Gridded vanes cases have not been developed for the field. This subsection provides a discussion of some of the results from the latest field test, as an example of typical validations performed.

Figure 12 shows data from the August 2015 field test in blue. These results were obtained using an anemometer at fixed azimuthal location (believed to be a ninety degree angle, where the zero is defined to be aligned with the streamwise flow direction) to measure the azimuthal velocity. The ultrasonic anemometer malfunctioned, and the temperature was only measured at one location at 1 meter height. A time series from approximately an hour was gathered. This data included large scenario uncertainties, with estimated 3

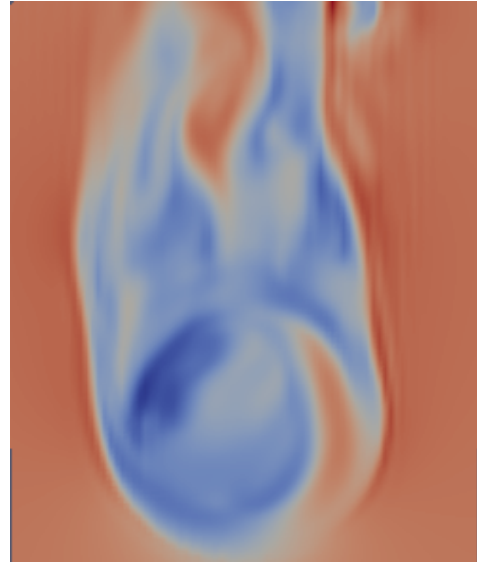
m/s variations in wind, 20 degree wind heading changes, and 10 degree Celsius shifts in temperature. A solidworks CAD file provided by the experimental team defined the vane and cone geometry, which were then represented in the simulations as virtual vanes and a solid surface, as described in Sections 3.4 and 3.5.

To span the range of conditions, several simulations were conducted with different scenario parameters. The azimuthal velocity from two such simulations (Red and Gold lines) are plotted against the experimental data (blue line) in Figure 12.

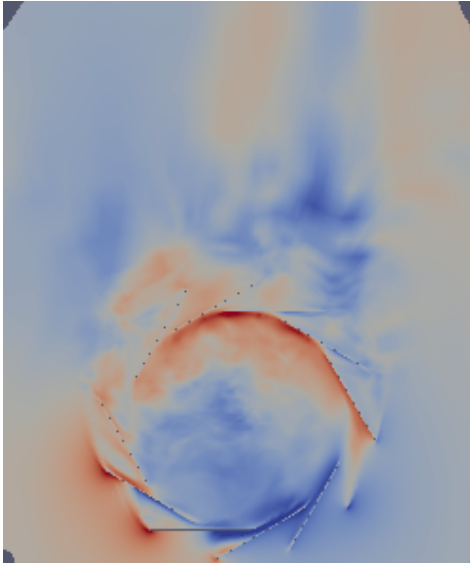
These simulations accurately bound the experimental data. Furthermore, a “Matching” case was identified that is broadly consistent with the field results. The kinetic energy flux, measured in a horizontal plane at the top of the vanes (where a turbine to extract this energy would likely be placed), in the simulations agrees with the experimental estimate within 10%.



(a) Streamwise Velocity: Gridded Vanes



(b) Streamwise Velocity: Virtual Vanes



(c) Spanwise Velocity: Gridded Vanes



(d) Spanwise Velocity: Virtual Vanes

Figure 11: Horizontal slices through the top of the vanes for the wind validation cases. On the left are the explicitly gridded vanes, and on the right the virtual vanes. The streamwise velocity shows penetration through the region where the vanes are aligned with the flow in both the gridded as well as virtual vanes. In addition, the virtual vane case correctly reproduces the direction and magnitude of the spanwise velocity inside the vanes. Finally, the wake has similar structure between the two cases.

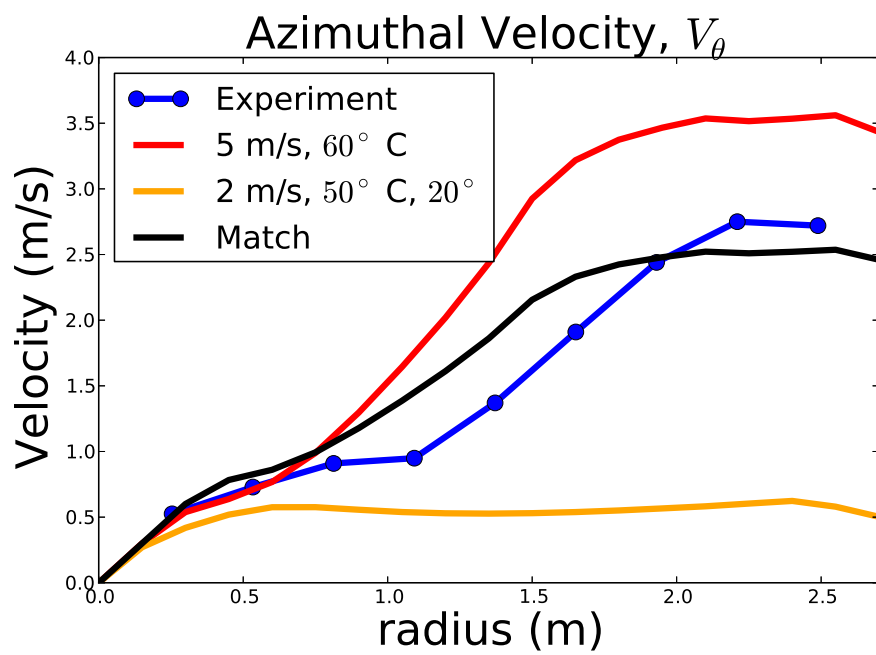


Figure 12: Azimuthal velocity data from the August 2015 field test is shown in blue. Two virtual vane simulations with different scenario parameters are shown in red and gold. The velocity field was temporally averaged but not averaged in space, to reproduce the measurements from the field.

## 6 Preliminary Results

The computer simulations in the proposed study are intended to discover the optimal solar vortex system configuration for a range of scenarios and system sizes. This section contains discussions of the preliminary simulation results to motivate that the existing simulation capability is sufficiently well developed and understood to permit an efficient exploration of the SoV configuration space. This section begins with a discussion of the structure of solutions from a representative case with no ambient winds, the “thermal only” scenario. Next, a case with strong ambient horizontal winds (“Wind”) is discussed. Finally, the results from a series of runs are shown to demonstrate a heuristic by which incremental optimization of the system configuration will be conducted.

### 6.1 Thermal Only

While ambient winds in the field impact system performance, it is also illuminating to consider an idealized scenario with natural convection driven only by thermal instabilities. Simulations of this baseline, thermal-only flow are intended to ensure the SoV apparatus to form a strong thermal plume even in the absence of wind.

In this subsection a representative case of an optimized thermal-only SoV configuration is presented. This is a simple curved vane configuration with two-tiers with ground temperature of 335 Kelvin and a freestream temperature of 313 Kelvin. There is no ambient velocity and the boundary conditions are as described in Section 3.8.

The two tiers of vanes used for these cases are drawn in Figures 13 and 14. Note that in the configuration, the vanes are aligned radially at the largest radius, and then increasingly curve towards azimuthal at smaller radius. Note that these are representative curves of the body forcing field, and do not actually represent vane surfaces. The vanes are represented as in Section 3.4. These images are created by tracing the path a particle follows through the forcing field. The region of forcing is between  $\{0.3 - 0.9\}$  meters for the bottom tier, and  $\{0.6 - 0.9\}$  meters for the top tier. Overall, the system is 1.1 meters tall, with the short first tier only standing 0.132 meters high. The top and bottom tiers have final angles of  $70^\circ$  and  $85^\circ$ , respectively. No cone is used in this case.

The results shown are the averages of fifty snapshots of the solution taken over the course of ten minutes. In general, the averaging times are selected to be approximately 20 to 30 wash-out times, where a wash-out is defined as the time required for a particle at the base of the apparatus to flow out through the top boundary. The kinetic energy flux through

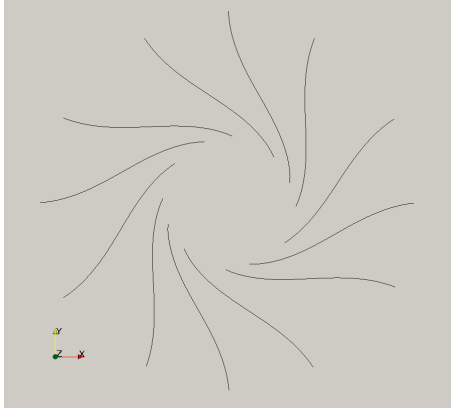


Figure 13: Horizontal drawings of the curvature functions for the bottom tier vanes. The max angle is  $85^\circ$ , or  $5^\circ$  less than azimuthal.

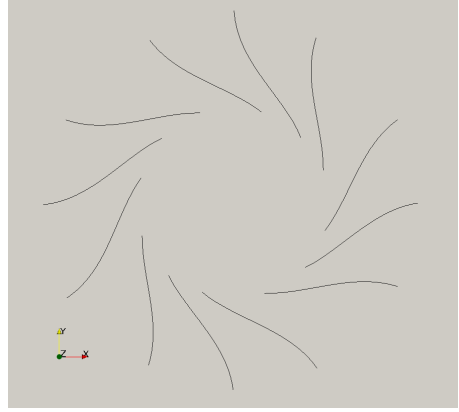


Figure 14: Horizontal drawings of the curvature functions for the top tier vanes. The max angle is  $70^\circ$ , or  $20^\circ$  less than azimuthal.

the top of the vanes for this case is about 53 watts. The solution demonstrates several features characteristic of naturally occurring dust devils. Figure 15 shows a temperature isocontour set at threshold of 3 Celsius higher than the ambient fluid temperature. This value was selected because it was noted by Sinclair[28] as characteristic of the thermal core temperature above the ambient temperature observed in dust devils. The image depicts a tight, coherent thermal plume roughly the same size as the inner diameter of the lower vanes. As anticipated, this hot flow is acting like a chimney, generating a large vertical velocity which in turn entrains air from the outside.

An image of the entrainment is shown in Figure 16. The image was created by tracking particles as they convect through the device. Tracer particles were seeded into the averaged flowfield and then advancing through the field using an RK4 time integrator. There is clearly a tight inner vortex with significant azimuthal velocity as well as a broader region of entraining fluid through the upper tier of vanes.

Figure 17 depicts several vertical slices through the SoV for various state variables. One can see that there is a tight core vortex with azimuthal and vertical velocities of several meters per second. The tight vortex region coincides with a high temperature, low pressure core region. The rapidly rotating air near the center induces a low pressure core, as observed in real dust devils. On the vertical velocity plot, a small downward flow region has formed in the middle of the vortex, consistent with the sketch in Figure 1.

Figure 18, depicts several horizontal slices through the SoV for the same state variables. It can be seen that the large velocities are highly localized to a region just inside the vanes.

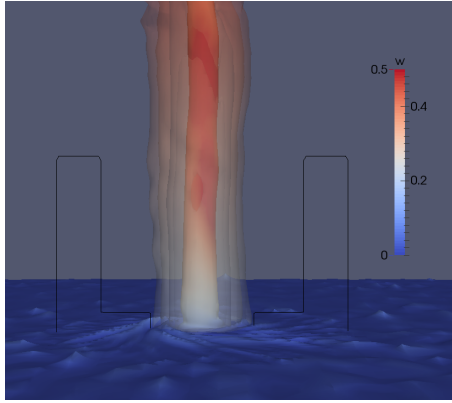


Figure 15: Isocountours of the inner thermal core visible through semi-transparent contour around azimuthal velocity, colored by vertical velocity. This shows that the thermal core creates an upward flow, which entrains and rotates fluid around it. An outline of the region of virtual vanes has been drawn.

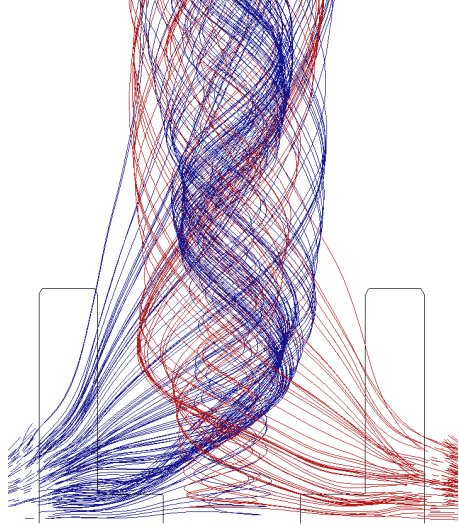


Figure 16: Fluid entrainment around the apparatus. This was drawn by seeding particles into the averaged flowfield and then advancing them using an RK4 time integrator. An outline of the virtual vanes are drawn to show the region of forcing.

Likewise, the entrainment of fluid is limited to a region immediately surrounding the vanes. Finally, the thermal plume is relatively narrow compared to the diameter of the device. It is desirable to broaden the thermal plume, as this would create a larger vertical momentum flux and consequently a larger kinetic energy flux. The diameter of the thermal core is therefore a critical flow characteristic in the thermal-only conditions. However, a means of setting the thermal plume's thickness is not presently known. Regardless, these slices lend credibility to the notion that our turning vane configuration is generating something with visible parallels to a naturally occurring dust devil.

## 6.2 Wind

The wind case is for a 5 m/s ambient wind with a ground temperature of 335 Kelvin and freestream temperature of 313 Kelvin. There is no ambient velocity and the boundary conditions are as described in Section 3.8. The vanes are drawn in Figures 19 and 20. These images show the straight vane case, as well as a cone that sits on top of the second tier of vanes. As in the previous section, these images are representative curves of the body forcing field, and do not actually represent vane surfaces. The vanes are represented as in Section

**3.4.** These images are created by tracing the path a particle follows through the forcing field. The region of forcing is between  $\{0.96 - 3.4\}$  meters for the bottom tier, and  $\{1.5 - 3.4\}$  meters for the top tier. Overall, the system is three meters tall, with the short first tier only standing 0.3 meters high. The top and bottom tiers have final angles of  $70^\circ$  and  $80^\circ$ , respectively.

Horizontal slices of the azimuthal and vertical velocities, as well as the temperature and pressure fields are shown in Figure 22b. The freestream velocity is traveling from left to right at  $5m/s$ , which was set based on ambient velocity measurements made by the experimental team from the field. While the structure is undoubtedly different than the thermal-only cases shown previously, we can nevertheless see that a thermal plume is forming along with a rotating velocity structure. In general the wind cases are more disorganized, with less obviously visible coherent structure. Notice however that the magnitude of velocities are several times larger than in the thermal-only cases, and the kinetic energy flux through the vanes is also significantly higher.

The vertical slices are shown in Figure 22. In this case, the lower tier of vanes are where the majority of flow is entering the center of the apparatus, while the second tier of vanes are blocking the ambient wind and providing protection for the vortex column.

The thermal plume is significantly less visible than in the thermal-only cases. While the thermal-plume is necessarily weaker relative to the wind, some of this is also due to the plume no longer being directly centered in the flow. The plume is more visible using isocountors to render a three-dimensional surface. To visualize the difference between the vertically varying ambient temperature and the warmer thermal plume, we use the potential temperature, defined as,

$$\tau(x, y, z) = T(x, y, z) - T_{in}(z) \quad (41)$$

where  $T_{in}$  is the inflow temperature, described in Section 3.8. In this way the background potential temperature is nearly zero, and larger values represent deviations from the base flow temperature. The isocountour of a three Kelvin is shown in Figure 23. This value was selected as it was noted as sufficient for formation of a dust devil by Sinclair[28]. It is clear from the image that a strong thermal column does exist even in the  $5m/s$  wind cases.

### 6.3 Optimization

In this section results from a representative optimization in a thermal-only case are discussed, to demonstrate the optimization process employed so far. This is a typical mode of sci-

tific and engineering inquiry, where a hypothesis regarding system operation is developed, followed by testing of the hypothesis, and further iterations.

This series of simulations are all runs with different system configurations conducted in a common ambient scenario, that of the unsteady thermal-only simulations described in Section 3.8.

Our objective is to maximize the energy that can be extracted from the synthetic dust devil. As a surrogate to this quantity, consider the kinetic energy flux through a horizontal plane near the top of the vanes, where a turbine will ultimately be placed. This is a surface integral[19]

$$\dot{E} = -\frac{\rho}{2} \int V_z(V_\theta^2 + V_z^2)dA. \quad (42)$$

Using the kinetic energy flux as an objective, the vane geometry has been optimized. Over approximately tens of iterations, we have increased the kinetic energy flux by a factor of 88 relative to the baseline. Major adjustments to design in the the vane shape and angles were made to obtain this improvement. Before and after images are shown in Figure 22a. During this optimization the qualitative character of the solution changed substantially, changing from a mild upward flow with little rotation to a strongly organized vortex with a downward central flow and strong azimuthal velocities. Before and after vertical slices are shown in Figure 25. Nevertheless, with a peak energy flux for the final iteration of less than one hundred Watts, significant further optimization is necessary for this system to be viable for use as an energy production system. This naturally leads to the next section, which is a discussion of the proposed research campaign.

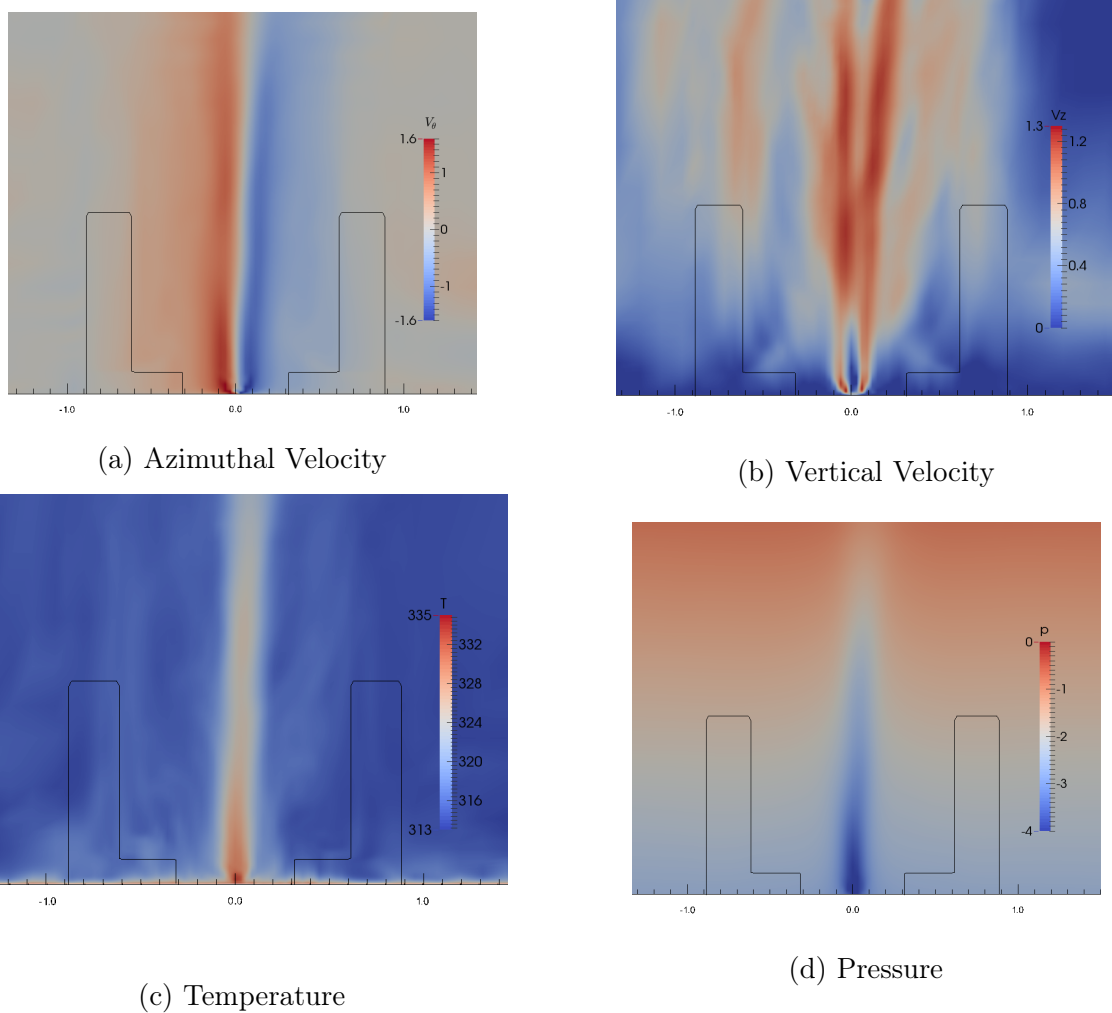


Figure 17: Time averaged vertical slices through the center of the device for the thermal-only cases. Black lines indicate the location of the vanes. A strong thermal plume is visible at the center of the device, which drives a vertical velocity. The fluid flow is entrained by this vertical movement and pulled radially into the center while being turned by the turning vanes. Notice also the low pressure “eye” at the center of the flow, as well as the modest downward flow in the center of the vertical velocity, consistent with Figure 1.

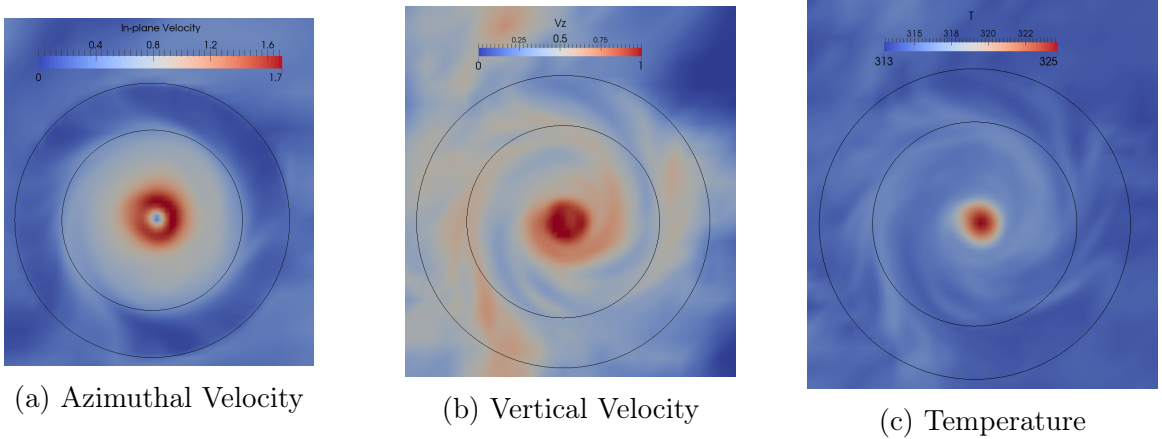


Figure 18: Time averaged horizontal slices taken at the height of the second tier of vanes for the thermal-only cases. These images show a clear thermal plume driving a strong vertical velocity. Notice also the low downward velocity “eye of the storm” in (a). In contrast to the wind cases, the vortex is well-anchored in the center of the apparatus.

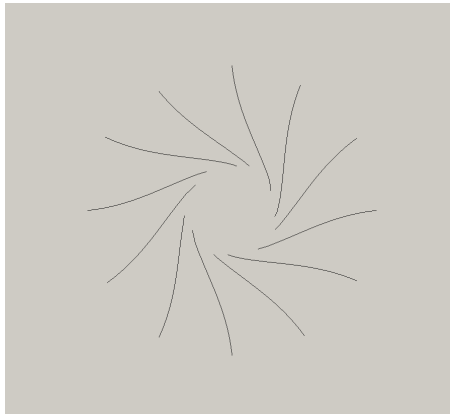


Figure 19: Horizontal drawings of the bottom tier vanes. These are curved vanes with a final angle of  $80^\circ$ .

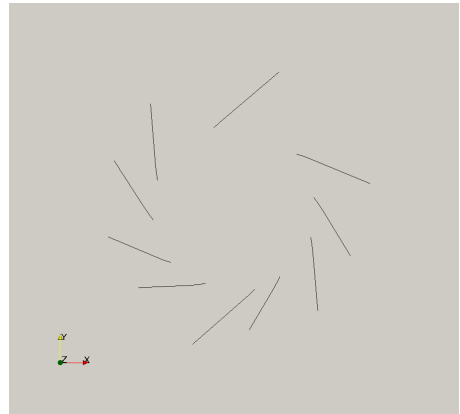
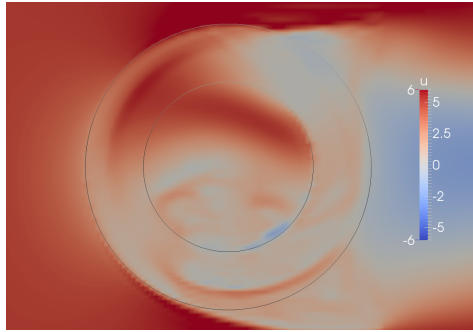
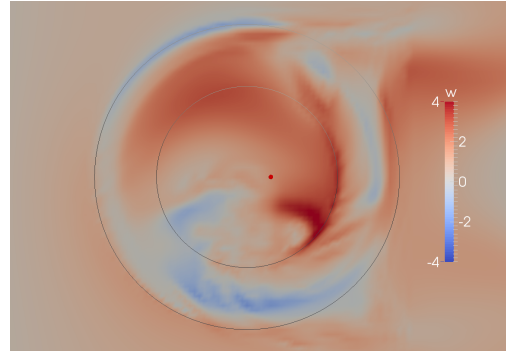


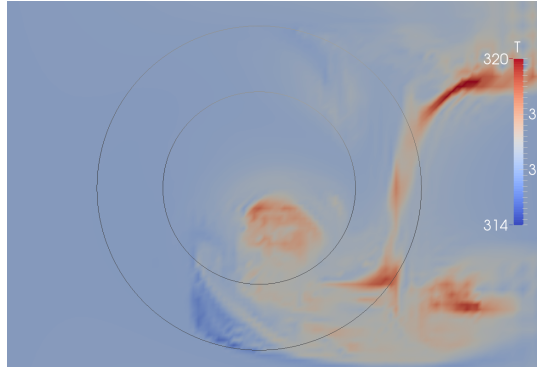
Figure 20: Horizontal drawings of the top tier vanes. These are straight angle vanes set at  $70^\circ$ .



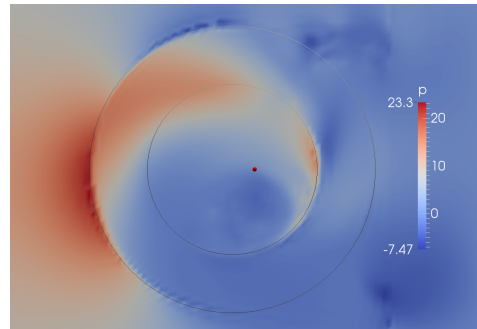
(a) Streamwise



(b) Vertical Velocity



(c) Temperature



(d) Pressure

Figure 21: Time averaged horizontal slices taken at the height of the vanes for the wind cases. The streamwise velocity shows a large penetration in the region where the vanes are not blocking, and in the other regions the flow is blocked and flows around. The vertical velocity is disorganized and does not show the “two cell” structure as in the thermal-only cases. Note that an off-center thermal plume is visible, as well.

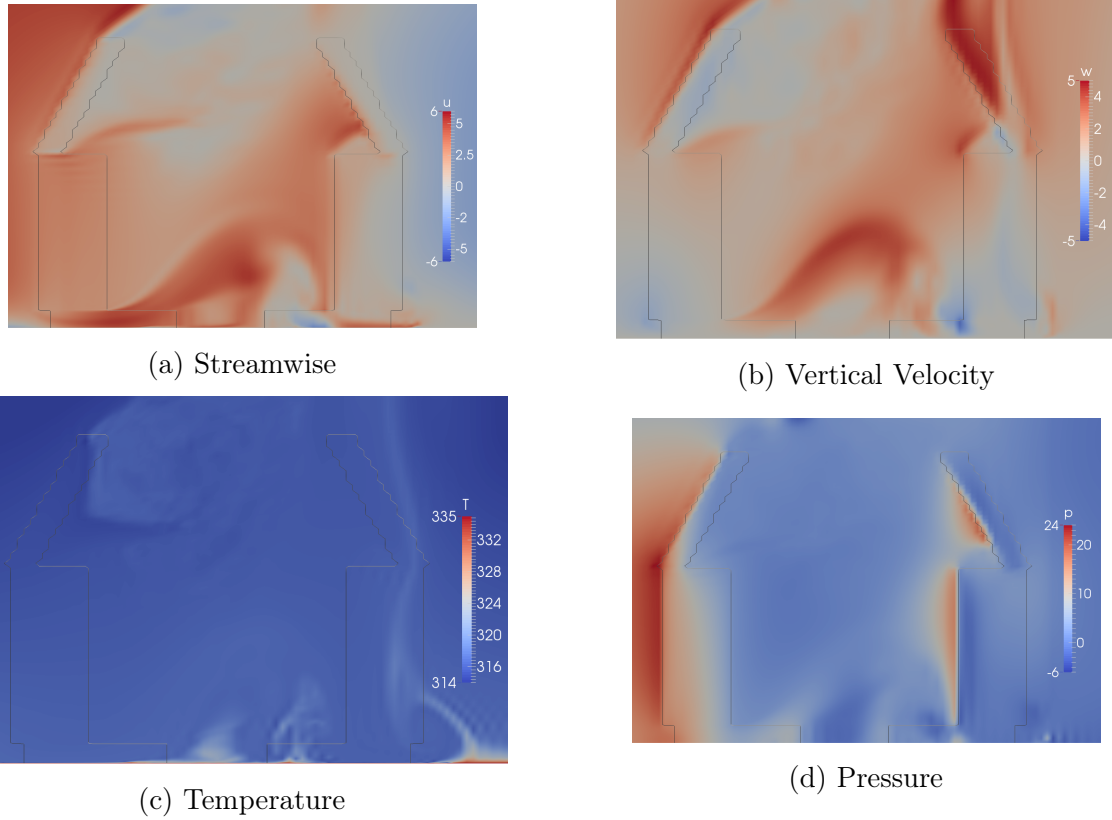


Figure 22: Time averaged vertical slices from the center of the device for the wind cases. A great deal of flow is radially entrained by the first tier of vanes, consistent with the approach proposed in Figure 2. Notice that while the temperature field appears to be quite modest, this is due to the fact that the thermal column is not well centered. The full column is quite visible in Figure 23.

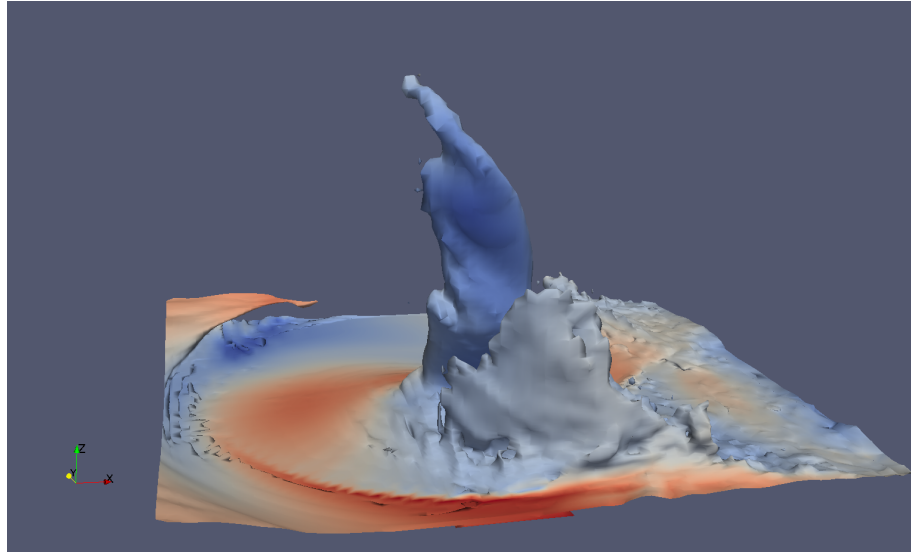


Figure 23: Iso-contour of the thermal plume. Here, the isocontour is labelled by the potential temperature,  $\tau$ , as defined in Equation 41. A strong thermal column has visibly formed. The figure is colored by the streamwise velocity, and shows the thermal column also has rotation.

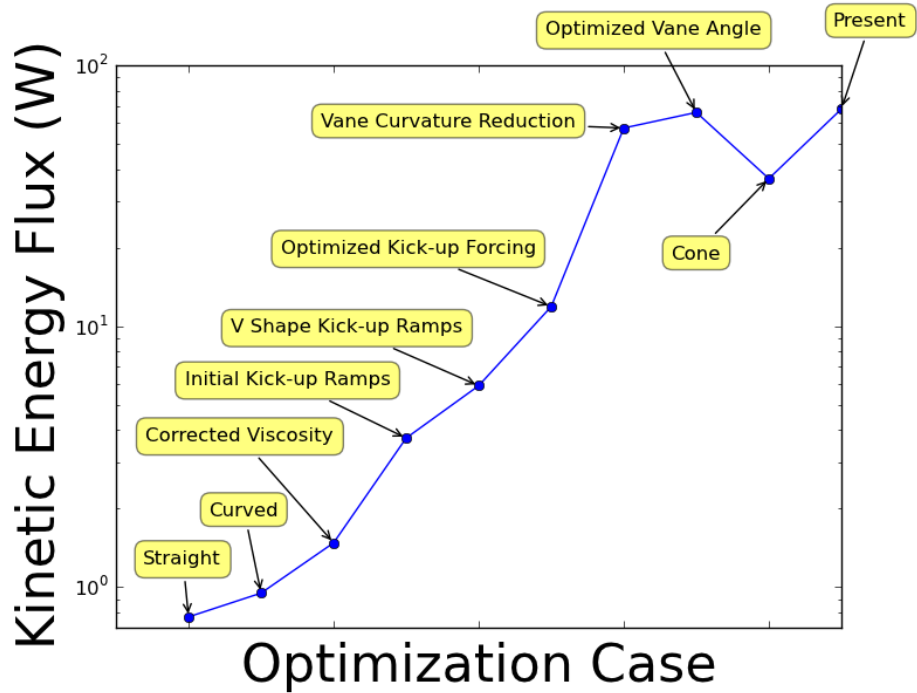


Figure 24: This plot diagrams the improvements to the calculated flux for each iteration of system configuration. Every iteration is labeled by design change.

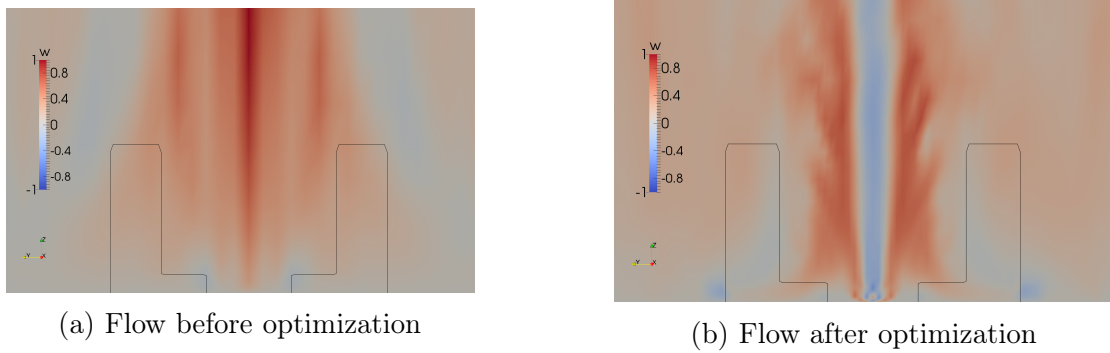


Figure 25: These are vertical slices taken at the center of the vanes of the vertical velocity taken before and after the numerous optimizations of the turning vanes detailed in Figure 24. In the original figure, the flow produces a narrow plume. In the second, the flow shows stronger vertical velocities in a much larger and more organized vortex. The flow has also transitioned into a “two-cell” structure akin to that observed in the naturally occurring phenomena as discussed in Section 2.1

## 7 Proposed Research Campaign

The objective of this research project is to provide a definitive assessment of the technological feasibility of the entire synthetic columnar vortex concept as a means of generating usable energy. In the previous sections outlined the present state of the simulation capability. In doing so, we have discussed the physics that influence dust devils formation, our particular mathematical models for the ambient conditions, as well as the SoV vanes, cone and turbine. We summarized the numerical discretizations used, the software stack and the calibration, verification and validation of these components. The purpose of these sections was to communicate two major points. The first is that an accurate, verified and validated simulation capability has been developed that can quickly investigate a wide variety of system and scenario settings at a modest computational cost. The second point is that we have developed heuristics that permit optimization of any baseline SoV configuration to a local maximum of energy production, as measured by kinetic energy flux through the top of the SoV vanes.

These two points justify the proposed course of work, which is to explore a large space of possible system configurations and geometries to discover the globally optimal structure of the SoV apparatus. Coupled with the scaling analysis presented in Section 2, we will then be able to predict the conditions (if any) under which the SoV apparatus will be technologically feasible. This will lead to investigating the physics of the apparatus, to assess how closely the synthetic dust devils mimic the natural variety. The proposed research is designed to assess feasibility, and it is not expected that actual experimental validation will accompany the computational results. Furthermore, it must also be emphasized that feasibility is focused on technical viability, namely energy produced by the apparatus, and will not include an economic assessment. In other words, it is possible that the SoV will produce energy, but the design required to do so is prohibitively expensive, and therefore not economically competitive with existing technologies. The following is a proposed program of simulations designed to explore a wide configuration space. This focuses on optimization for the cone, turbine and vanes.

The three cone parameters we propose to optimize are shown in Table 2. We expect to optimize the cone after the bottom and top tiers are adjusted. For the cone, we expect the height, maximum diameter and inner exit diameter to all impact the flow. While it is not known what form the ideal cone geometry will take, our expectation is that the cone plays at least two important roles. The first is acting as a converging nozzle for the flow, increasing the vertical and azimuthal velocity as it exits out the top of the device. In the wind, the cone also acts as a shield, preventing the high velocity freestream flow from disrupting the

vortex before it has run through the turbine.

Parameter	Description	Range
$H_C/D_C$	Ratio of the height of the cone versus the cone diameter	( 0 - 2.0 )
$D_C/D$	Ratio of the cone diameter versus the system diameter	( 0.5 - 1.5 )
$D_{\text{out}}/D_C$	Ratio of the cone exit diameter versus the cone diameter	( 0.25 - 1.0 )

Table 2: Cone Optimization Parameters.

The turbine parameters to be optimized are shown in Table 3. In addition to these configuration parameters, the location of the turbine will likely need to be optimized to be centered on the vortex, which may not be centered inside the vanes due to asymmetric effects of wind, vane geometry, etc.

Parameter	Description	Range
$N_B$	Number of blades	( 1 - 12 )
$I$	Moment of inertia	( 1 - 12 )
$r_B/r_{\min}^t$	Radius of blade versus the inner radius of the top tier vanes	( 0 - 1 )
$H_B/H$	Height of the turbine blades versus system height	( 0 - 1.2 )

Table 3: Proposed Turbine Optimization Parameters.

The possible configuration space for the vanes is much larger. Presently, the workflow consists of weekly calls with the experimental team to discuss possible system designs, which typically consist of vane sketches or drawings. One such proposed design is shown in Figure 26. These vanes are highly asymmetric with variation in the length and curvature as a function of spatial location. Furthermore, in this design the down wind side of the apparatus is enclosed by a solid cylindrical wall. While the vane representation outlined in Section 3.4 is expected to be sufficiently general to support a wide variety of vane configurations, it is not at this time clear what form of parameterization for vane angle is sufficiently general to support this exploration, and so a table like that for the cone and turbine is not yet available. At present the expectation is to proceed with this conceptual phase to generate a wide range of possible configurations. The designs that have initially promising results will then be

optimized similar to the examples outlined in Section 6, where new parameter values are introduced, a run is performed, and then the output is postprocessed and evaluated before the process begins again. In this way it is not infeasible to expect that several hundred optimization runs can be performed.

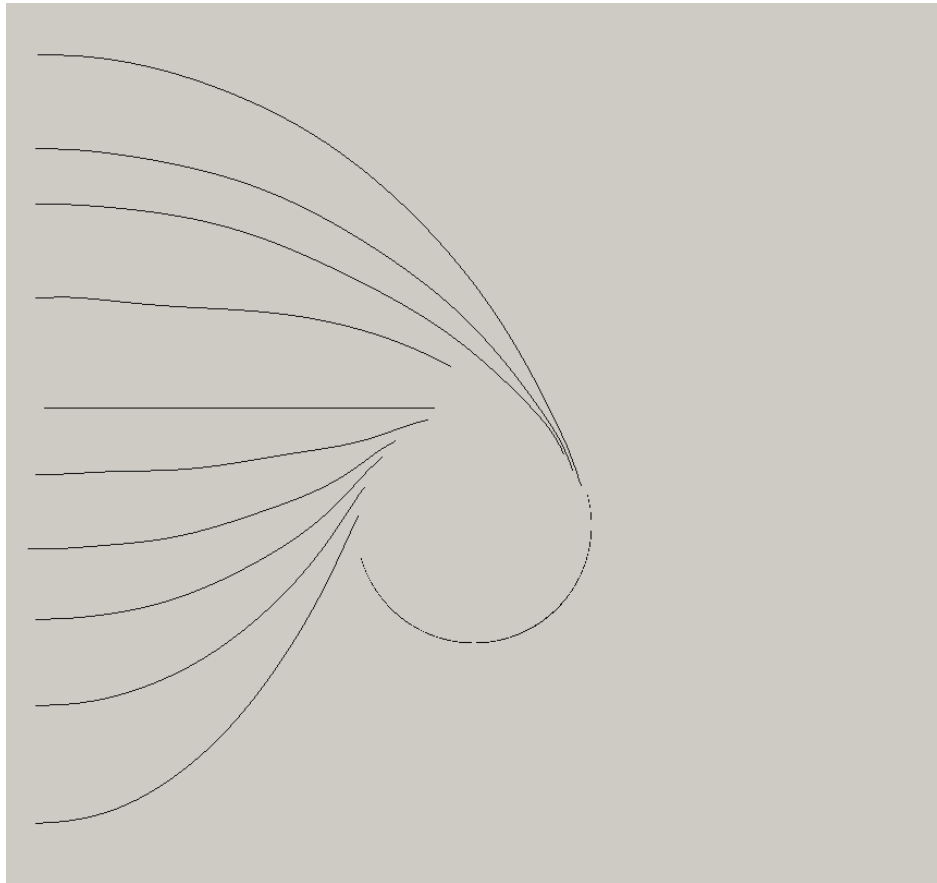


Figure 26: This is an example image of a proposed vane design. The lines indicate the vane curvature and solid surfaces. Sketches and diagrams such as this are typically generated by various members of the team. The vane surface is then instantiated as a region of forcing as detailed in Section 3.4 and then simulated. If the initial results are promising, then further exploration of that configuration may be pursued.

## 7.1 Proposed Timeline

A timeline for the proposed work is presented in Table 7.1. The date of each bullet is the planned completion of the deliverable. Bullets items in black are required, while those in blue are optional, and do not need to be completed to ensure the success of this project.

The first bullet in Table 7.1 provide estimated ending dates for the exploration of the configuration space. We have rapidly iterated through these optimization efforts over the course of several months, and are nearly converged on a final design. The second bullet relates to the the final verification of the turbine, to ensure this functions properly. At this time we will proceed with “coupling tests” to ensure that the parameters are indeed still appropriate. For example, after having optimized the turbine parameters, it may be necessary to perturb the lower tier vane parameters to ensure that the selected set is nearly optimal even with the addition of a turbine.

The third bullet is the expected deadline to provide the results of our computational simulation efforts to the experimental group in late Spring/early Summer of 2016 so that they can use this information in the design of the system to be used for the Arizona field tests in Summer, 2016. The date of the actual field test has not yet been set and may change.

As mentioned in the fourth item, it is possible that this project will permit some glimpses at the fundamental processes underlying the naturally dust devil phenomena. To accomplish this, the synthetic dust devils must be compared to data from the naturally occurring variety, with some appropriate scaling. While it is not a significant component of the proposal, this and several simple investigations into related phenomena such as tornados and hurricanes will also be investigated. A literature review of the physics of general cyclonic structures and any observed intensification mechanisms may provide hints of the geometries by which the flow is intensified, and why.

Given our previous experiences, we do not anticipate a rich validation data set to be available after the field test. Nevertheless, we will postprocess any and all available data from this event in order to assess the reliability of the computational modeling efforts.

Finally, we anticipate a detailed accounting of the entire project as the final deliverable. We expect that all of the investigations detailed above will result in several publications, as well.

Table 4: Timeline of proposed work. Bullets are dates of planned completion of deliverables. Black items are requisite, blue optional.

<b>April 2016</b>	Conclude parameter sweeps and optimization of apparatus.
<b>April 2016</b>	Turbine actuator-disk verification, validation and prediction.
<b>May 2016</b>	Proposed configuration and predictions for experimental team.
<b>July 2016</b>	Comparisons between synthetic and natural dust devil physics.
<b>Aug 2016</b>	Validation against 2016 field data.
<b>Fall 2016</b>	Doctoral dissertation writing.

## A Course list

Course Number	Semester	Course Name	Instructor
ME381P	2014 Spring	Validation and Uncertainty Quantification	Prof. R.D. Moser
ME 382R5	2014 Spring	Advanced Combustion	Prof. O.A. Ezekoye
CSE 397	2014 Spring	Comp. & Var. Methods for Inv. Problems	Prof. O. Ghattas
SDS 384	2014 Fall	Bayesian Statistical Methods	Prof. S. Walker
SDS 394	2014 Fall	Scientific & Technical Computing	Dr. V. Eijkhou
ME 382P	2015 Fall	Advanced Exp. Methods in Thermal/Fluids	Prof. D. Bogard

## B Stabilization and Weak Formulation

This appendix details the weak formulation of the Navier Stokes equations instantiated in the software GRINS, as well as providing a derivation of the  $\tau$  stabilization terms.

In brief, our process is the following:

- Cast Navier Stokes + Boussinesq equations into weak form
- Prepare as an operator  $Lc = f$
- Calculate Fréchet derivative
- Separate into differential (P) and constant (Z) components,  $L'[c] = P + Z$
- Choose stabilization operator such that  $S = -P^*$
- Then stabilization has form,  $a_h(c, \phi) = a(c, \phi) + \langle Lc, S\phi \rangle_\tau$

This is essentially the least-squares stabilization proposed by Hughes and extended to natural convection by Becker and Braack.

### B.1 Weak Formulation of Equations of Interest

We begin with the incompressible Navier-Stokes equations with Bousinesq buoyancy,

$$\nabla \cdot u = 0 \tag{43}$$

$$\frac{\partial u}{\partial t} + u \cdot \nabla u = -\frac{1}{\rho} \nabla p + \nu \nabla^2 u + g \frac{T'}{T_0} \tag{44}$$

$$\rho c_p \frac{\partial T}{\partial t} + u \cdot \nabla T = \nabla \cdot (k \nabla T) \tag{45}$$

e.g. the continuity, momentum and energy equations, respectively. Our state vector is  $c = [p, u, T]$ . To cast these into weak form we multiply by appropriate test functions  $\phi = [q, v, w] \in H_0^1(\Omega)$  and integrate over the domain,  $\Omega \in \mathbb{R}^n$ . Our system of equations now

appears as,

$$\int_{\Omega} q \nabla \cdot u \, dx = 0 \quad (46)$$

$$\int_{\Omega} \dot{u} \cdot v \, dx + \int_{\Omega} (u \cdot \nabla) u \cdot v \, dx = \int_{\Omega} \frac{p}{\rho} \nabla \cdot v \, dx - \nu \int_{\Omega} \nabla u \cdot \nabla v \, dx + \int_{\Omega} g \frac{T'}{T_0} \cdot v \, dx \quad (47)$$

$$\rho c_p \int_{\Omega} \dot{T} \cdot w \, dx + \int_{\Omega} (u \cdot \nabla) T \cdot w \, dx = - \int_{\Omega} (k \nabla T) \cdot \nabla w \, dx \quad (48)$$

where an “over-dot” denotes time differentiation, e.g.  $\dot{u} = \frac{\partial u}{\partial t}$ . Note that both the pressure term as well as the viscous term were integrated by parts to reduce the required order of the solution on those state variables.

We define the inner product by the shorthand notation  $(u, v) = \int_{\Omega} u \cdot v \, dx$ , giving our equations the form,

$$(\nabla \cdot u, q) = 0 \quad (49)$$

$$(\dot{u}, v) + (u \cdot \nabla u, v) - (p, \nabla \cdot v) + \nu(\nabla u, \nabla v) = (g \frac{T'}{T_0}, v) \quad (50)$$

$$\rho c_p (\dot{T}, w) + (u \cdot \nabla T, w) + (k \nabla T, \nabla w) = 0. \quad (51)$$

This defines our weak form operator  $a(c, \phi)$ . Our full equations will also include a stabilization term such that,

$$a_h(c, \phi) = a(c, \phi) + \langle Lc, S\phi \rangle_{\tau}. \quad (52)$$

The subsequent section will define the operators  $L$  and  $S$ , so that we might then fully define the stabilization term  $\langle Lc, S\phi \rangle_{\tau}$ .

## B.2 The operators $L$ and $S$

To form the stabilization terms,

$$\langle Lc, S\phi \rangle_{\tau} \quad (53)$$

we must define the operators  $L$  and  $S$ . The operator  $L$  is simply the PDEs in Equations

43 - 45 written in operator form. S is defined as the negative adjoint of the differential terms in L, e.g.

$$L'[c] = P + Z \quad (54)$$

$$S = -P^*. \quad (55)$$

Where P are the differential terms, and Z the constant terms.

Our objective is now to construct the adjoint operator of L. This is accomplished using the Fréchet derivative, which defines the functional derivative on L. In general this is accomplished by taking the first variation of a function  $\Pi(u)$  around a base state,  $u$ ,

$$\delta \Pi(u) = \lim_{\epsilon \rightarrow 0} \frac{\Pi(u + \epsilon \hat{u}) - \Pi(u)}{\epsilon} = \frac{\partial \Pi(u + \epsilon \hat{u})}{\partial \epsilon} \Big|_{\epsilon=0} \quad (56)$$

for all  $\hat{u}$  and  $\epsilon > 0$  with  $u + \epsilon \hat{u} \in H_0^1(\Omega)$ . This is recognizable as the Gâteaux derivative of the functional.

We now consider the first variation of state for the momentum equation term by term. The convective term is,

$$\frac{\partial}{\partial \epsilon} (u + \epsilon \hat{u}) \cdot \nabla (u + \epsilon \hat{u}) \quad (57)$$

$$= \lim_{\epsilon \rightarrow 0} \hat{u} \cdot \nabla (u + \epsilon \hat{u}) \quad (58)$$

$$= \hat{u} \cdot \nabla u \quad (59)$$

$$= -u \cdot \nabla \hat{u} \quad (60)$$

and the viscous term is,

$$\frac{\partial}{\partial \epsilon} \nabla^2 (u + \epsilon \hat{u}) \quad (61)$$

$$= \nabla^2 \hat{u} \quad (62)$$

while the buoyancy term is,

$$\delta \left( -g \frac{T'}{T_0} \right) = \delta \left( -g \frac{T - T_0}{T_0} \right) \quad (63)$$

$$= -g \frac{\partial}{\partial \epsilon} \left( \frac{T - T_0 + \epsilon \hat{T}}{T_0} \right) \quad (64)$$

$$= -g \left( \frac{\hat{T}}{T_0} \right) \quad (65)$$

and thus the full adjoint equation for momentum appears as

$$-u \cdot \nabla \hat{u} - \nabla^2 \hat{u} = -\frac{1}{\rho} \nabla p. \quad (66)$$

The continuity equation is straightforward,

$$\frac{\partial}{\partial \epsilon} \nabla \cdot (u + \epsilon \hat{u}) = 0 \quad (67)$$

$$\nabla \cdot \hat{u} = 0. \quad (68)$$

Finally, consider the convective term of the energy equation,

$$\frac{\partial}{\partial \epsilon} u \cdot \nabla (T + \epsilon \hat{T}) = u \cdot \nabla \hat{T} \quad (69)$$

and the thermal diffusion term,

$$\frac{\partial}{\partial \epsilon} \cdot (-k \nabla (T + \epsilon \hat{T})) = \nabla \cdot (-k \nabla \hat{T}). \quad (70)$$

The full adjoint energy equation is therefore,

$$u \cdot \nabla \hat{T} + \nabla \cdot (k \nabla \hat{T}) = 0. \quad (71)$$

We are now in a position to define the matrices L and S. L comes directly from the PDEs in Equations 43 - 45 and is defined as thus,

$$L = \begin{pmatrix} 0 & \nabla \cdot () & 0 \\ \nabla () & u \cdot \nabla () - \nu \nabla^2 () & -g \frac{()}{T_0} \\ 0 & 0 & u \cdot \nabla () - \nabla \cdot (k \nabla ()) \end{pmatrix}. \quad (72)$$

While the S matrix is constructed from Equations 66, 68, and 71 must be,

$$S = -P^* = \begin{pmatrix} 0 & \nabla \cdot () & 0 \\ \nabla () & u \cdot \nabla () + \nu \nabla^2 () & -g \frac{()}{T_0} \\ 0 & 0 & u \cdot \nabla () + \nabla \cdot k \nabla () \end{pmatrix}. \quad (73)$$

### B.3 Tau stabilization terms

Finally, we may now form the  $\tau$  stabilization terms,

$$\langle Lc, S\phi \rangle_\tau. \quad (74)$$

Where the operator  $\langle \cdot, \cdot \rangle_\tau.$  is shorthand and denotes

$$\langle u, v \rangle_\tau = \sum_K \tau_K(u, v)_K. \quad (75)$$

Where  $K$  denotes the FEM cells. Now, through what Becker and Braack contemptibly referred to as “elementary calculus”, we now discover our stabilization terms,

$$\begin{aligned} \langle Lc, S\phi \rangle_\tau = & \sum_K \{ \tau_p(\nabla \cdot u, \nabla \cdot v) \\ & + \tau_u(\nabla p + u \cdot \nabla u - \nu \nabla^2 - g \frac{T'}{T_0}, \nabla q) \\ & + \tau_u(\nabla p + u \cdot \nabla u - \nu \nabla^2 - g \frac{T'}{T_0}, \nabla u \cdot \nabla v + \nu \nabla^2 v) \\ & + \tau_T(u \cdot T - \nabla \cdot (k \nabla T), \nabla u \cdot \nabla w + \nabla \cdot (k \nabla w)) \}. \end{aligned}$$

## References

- [1] Annual Energy Outlook 2015. Technical report, U.S. Department of Energy, 04 2015.
- [2] Ivo Babuška. The finite element method with penalty. *Mathematics of Computation*, 27(122):pp. 221–228, 1973.
- [3] Matt Balme and Ronald Greeley. Dust devils on earth and mars. *Reviews of Geophysics*, 44(3):n/a–n/a, 2006.
- [4] P. T. Bauman and R. H. Stogner. Grins: A multiphysics framework based on the libmesh finite element library. submitted, <http://arxiv.org/abs/1506.06102>.
- [5] Roland Becker and Malte Braack. Solution of a stationary benchmark problem for natural convection with large temperature difference. *International Journal of Thermal Sciences*, 41(5):428 – 439, 2002.
- [6] Bert Blocken, Ted Stathopoulos, and Jan Carmeliet. {CFD} simulation of the atmospheric boundary layer: wall function problems. *Atmospheric Environment*, 41(2):238 – 252, 2007.
- [7] Howard B. Bluestein, Christopher C. Weiss, and Andrew L. Pazmany. Doppler radar observations of dust devils in texas. *Monthly Weather Review*, 132(1):209–224, Jan 2004.
- [8] A. N. Brooks and T. J. R. Hughes. Streamline upwind/petrov-galerkin formulations for convection dominated flows with particular emphasis on the incompressible navier-stokes equations. *Comput. Methods Appl. Mech. Eng.*, pages 199–259, September 1990.
- [9] Tim Colonius. Modeling artificial boundary conditions for compressible flow. *Annual Review of Fluid Mechanics*, 36(1):315–345, 2004.
- [10] P.A. Durbin and B.A.P. Reif. *Statistical theory and modeling for turbulent flows*. Wiley, 2001.
- [11] Roger Edwards, James G. Ladue, John T. Ferree, Kevin Scharfenberg, Chris Maier, and William L. Coulbourne. Tornado intensity estimation past, present, and future.
- [12] Thomas Foken. 50 years of the monin–obukhov similarity theory. *Boundary-Layer Meteorology*, 119(3):431–447, 2006.

- [13] M.D. Gunzburger. *Finite element methods for viscous incompressible flows: a guide to theory, practice, and algorithms*. Computer science and scientific computing. Academic Press, 1989.
- [14] Douglas V. Hoyt. A model for the calculation of solar global insolation. *Solar Energy*, 21(1):27 – 35, 1978.
- [15] Thomas J.R. Hughes, Leopoldo P. Franca, and Marc Balestra. A new finite element formulation for computational fluid dynamics: V. circumventing the babuška-brezzi condition: a stable petrov-galerkin formulation of the stokes problem accommodating equal-order interpolations. *Computer Methods in Applied Mechanics and Engineering*, 59(1):85 – 99, 1986.
- [16] T.J.R. Hughes. *The Finite Element Method: Linear Static and Dynamic Finite Element Analysis*. Dover Civil and Mechanical Engineering. Dover Publications, 2000.
- [17] Katharine M. Kanak. Numerical simulation of dust devil-scale vortices. *Quarterly Journal of the Royal Meteorological Society*, 131(607):1271–1292, 2005.
- [18] B. S. Kirk, J. W. Peterson, R. H. Stogner, and G. F. Carey. libMesh: A C++ Library for Parallel Adaptive Mesh Refinement/Coarsening Simulations. *Engineering with Computers*, 22(3–4):237–254, 2006. <http://dx.doi.org/10.1007/s00366-006-0049-3>.
- [19] L. D. Landau, E. M. Lifshitz, J. B. Sykes, and W. H. Reid. *Fluid Mechanics*. Pergamon Press Oxford, England, 1959.
- [20] Rajat Mittal and Gianluca Iaccarino. Immersed boundary methods. *Annual Review of Fluid Mechanics*, 37(1):239–261, 2005.
- [21] P. Moin. *Fundamentals of Engineering Numerical Analysis*. Cambridge University Press, 2010.
- [22] A. S. Monin and A. M. Obukhov. Basic laws of turbulent mixing in the surface layer of the atmosphere. *Contributions of the Geophysical Institute of the Slovak Academy of Sciences*, 24(151):163–187, 1954.
- [23] A.S. Monin, A.M. I?A?glom, and J.L. Lumley. *Statistical Fluid Mechanics: Mechanics of Turbulence*. Number v. 1 in Dover books on physics. Dover Publications, 2007.

- [24] B.R. Munson, A.P. Rothmayer, and T.H. Okiishi. *Fundamentals of Fluid Mechanics, 7th Edition*. John Wiley & Sons, Incorporated, 2012.
- [25] T.R. Oke. *Boundary Layer Climates*. Vie juridique des peuples [par la] Bibliothèque de droit contemporain. Routledge, 1987.
- [26] S.B. Pope. *Turbulent Flows*. Cambridge University Press, 2000.
- [27] J. A. Ryan and J. J. Carroll. Dust devil wind velocities: Mature state. *Journal of Geophysical Research*, 75(3):531–541, 1970.
- [28] Peter C. Sinclair. General characteristics of dust devils. *Journal of Applied Meteorology*, 8(1):32–45, Feb 1969.
- [29] Peter C. Sinclair. The lower structure of dust devils. *Journal of the Atmospheric Sciences*, 30(8):1599–1619, Nov 1973.
- [30] L. Tobiska. Carey, g. f.; oden, j. t. (eds.), finite elements: Fluid mechanics. vol. vi. (the texas finite element series 6). *ZAMM - Journal of Applied Mathematics and Mechanics / Zeitschrift für Angewandte Mathematik und Mechanik*, 68(9):458–459, 1988.
- [31] Anthony D. Toigo, Mark I. Richardson, Shawn P. Ewald, and Peter J. Gierasch. Numerical simulation of martian dust devils. *Journal of Geophysical Research: Planets*, 108(E6):n/a–n/a, 2003. 5047.
- [32] R. E. Wilson and P. B. S. Lissaman. Applied aerodynamics of wind power machines. *NASA STI/Recon Technical Report N*, 75:22669, July 1974.
- [33] Y. Z. Zhao, Z. L. Gu, Y. Z. Yu, Y. Ge, Y. Li, and X. Feng. Mechanism and large eddy simulation of dust devils. *Atmosphere-Ocean*, 42(1):61–84, 2004.